Check for updates

A roadmap for the commercialization of perovskite light emitters

Tae-Hee Han[1,6], Kyung Yeon Jang[2,6], Yitong Dong[3], Richard H. Friend[4], Edward H. Sargent[3] and Tae-Woo Lee[2,5] ✉

Abstract | Metal halide perovskites (MHPs) possess advantageous optoelectronic properties, so perovskite emitters and perovskite light-emitting diodes (PeLEDs) are promising candidates for next-generation high-colour-purity displays and lighting applications. Within the past 5 years, the luminescence efficiency of MHP emitters and PeLEDs has increased rapidly. However, the industrial applications of perovskites are impeded by several technical bottlenecks, such as insufficient colour reproducibility, low operational stability, toxicity and limited large-scale production. In this Review, we survey the current status of MHP emitters and PeLEDs and provide a technical roadmap to highlight the goals and requirements for them to successfully enter the markets for vivid displays with high colour purity, augmented and virtual reality displays and general and special lighting. We also set out steps for future research in MHPs and their device applications.

[1]Division of Materials Science and Engineering, Hanyang University, Seoul, Republic of Korea.

[2]Department of Materials Science and Engineering, Seoul National University, Seoul, Republic of Korea.

[3]Department of Electrical and Computer Engineering, University of Toronto, Toronto, Ontario, Canada.

[4]Cavendish Laboratory, University of Cambridge, Cambridge, UK.

[5]School of Chemical and Biological Engineering, Institute of Engineering Research, Research Institute of Advanced Materials, Soft Foundry, Seoul National University, Seoul, Republic of Korea.

[6]These authors contributed equally: Tae-Hee Han, Kyung Yeon Jang.

✉e-mail: twlees@snu.ac.kr

https://doi.org/10.1038/s41578-022-00459-4

Displays have become a core technology for human convenience in the current information society. Light-emitting diodes (LEDs) are essential parts of display technology; they need to have high colour purity, high luminescence efficiency, high resolution and long-term stability. In present displays, organic light-emitting diodes (OLEDs) offer high efficiency and long lifetime and are widely used in various display markets such as mobile phones and televisions. OLEDs possess relatively broad photoluminescence (PL) and electroluminescence (EL) spectra: the full width at half maximum (FWHM) of their emission is generally larger than 45 nm (REF.[1]), which represents around 85% of the colour gamut required by the National Television System Committee and about 65% of the colour space required by the ITU-R Recommendation BT.2020 (Rec.2020) for 4K and 8K ultra-high definition television standard, based on the chromaticity diagram from the Commission internationale de l'éclairage (CIE)[1]. Currently, commercial OLEDs are produced using vacuum evaporation, which entails high cost to fabricate a multilayered structure of OLED stacks. Inorganic colloidal quantum dots (QDs) have also been used for colour-conversion in liquid crystal displays (LCDs). Although QDs can provide a colour gamut of over 110% of the National Television System Committee standard with FWHM of around 30 nm, this is still insufficient to meet the colour standard required in high-colour-purity displays (about 85% of Rec.2020)[1,2]. Other disadvantages of QDs, such as their expensive and complex synthesis, remain obstacles to wide application[2].

Metal halide perovskites (MHPs) have narrowband emission (with FWHM of about 35 nm for red[3–5] and about 20 nm for green[6–8] and blue[9,10]) and an easily tuneable bandgap (with an emission range of 410–850 nm), so they are regarded as promising candidates for applications such as high-colour-purity displays, biomedical imaging and surveillance[1,6,11–14]. The market share of high-end OLED and micro-LED televisions with high resolution and colour purity has continuously increased despite their high price, indicating an increasing consumer demand for more vivid displays[15]. MHPs are the only emitters that can fully satisfy the required colour gamut (Rec.2020) for ultra-high definition displays at low cost[16].

OLEDs and quantum dot LEDs (QD-LEDs) have been developed for display technologies for around 20 years. By contrast, perovskite light-emitting diodes (PeLEDs) have been investigated for only a few years. However, the external quantum efficiency (EQE) of PeLEDs has increased much more rapidly than that of OLEDs and QD-LEDs. The commercialization of PeLEDs is challenging; their insufficient operational stability is one of the biggest issues, together with the need to develop environmentally friendly synthesis routes for MHPs and large-scale production methods.

This Review identifies key challenges in the development of MHP materials and PeLEDs towards commercialization by considering the needs of the consumer electronics market and the demands for PeLEDs at the industrial level. We propose a technical roadmap for research on PeLEDs, targeting the technological

evolution of materials and devices towards applications to guide research in this emerging field.

Current status of metal halide perovskites

In MHPs, the conduction band minimum (CBM) is formed by the unoccupied Pb 6*p*-halide n*s* antibonding orbitals (such as Cl 3*s*, Br 4*s* and I 5*s*; n is the principal quantum number) and is mostly affected by the Pb *p* orbital, whereas the valence band maximum (VBM) is composed of the filled Pb 6*s*-halide n*p* antibonding orbitals (such as Cl 3*p*, Br 4*p* and I 5*p*)[17–19]. These properties enable easy bandgap tuning by substituting halides[20]. Also, MHPs form a direct bandgap that enables a high absorption coefficient ($>10^5\,cm^{-1}$)[21], a high PL quantum yield (PLQY; close to 1)[22] and a high PeLED EL efficiency.

Bulk MHPs have an exciton binding energy as low as a few tens to hundreds of millielectronvolts (26–150 meV)[23], and a carrier diffusion length longer than 1 μm, much longer than in organic materials (about 10 nm)[24,25]. This long diffusion length can be a disadvantage in light-emitting applications owing to increased nonradiative recombination caused by deep-level traps at the MHP surface or at device interfaces, because PeLEDs have a thickness of only a few hundred nanometres[13,26,27]. Methods of increasing the binding energy and the radiative recombination rate include the formation of layered 2D MHPs, which results in charge-carrier confinement by reducing the 3D MHP's crystal size[13,28]. At room temperature, the linewidth of the PL spectrum of MHPs with polar Pb–halide bonds is affected mainly by the couplings between charge carriers and longitudinal optical phonons via Fröhlich interactions rather than by impurities or defects[29,30]. Therefore, MHPs whose emission depends on their crystal structures and compositions can have a low FWHM of around 20 nm that is relatively insensitive to the crystal size and to intrinsic defects.

The luminescence efficiencies of PeLEDs based on MHP emitters have increased rapidly (FIG. 1a). The evolution of the EQE of PeLEDs can be divided into three stages. In the first stage, the luminescence of PeLEDs at room temperature was too dim to be measured. This changed when the first bright PeLED (300–400 cd m^{-2}) with a low EQE of about 0.1% was demonstrated in 2014, using polycrystalline MHPs (grain size >100 nm)[29,31]. Following that, a PeLED with a EQE of about 8% was achieved by reducing the grain size in 2015 (REF.[13]), opening up the second stage of PeLED development, with EQEs of around 10%. In 2018, the third stage started, with the development of PeLEDs possessing EQEs of about 20% through the development of defect-passivated polycrystalline MHP films[32,33], synthesis and ligand-engineering strategies for nanocrystals[4] and the use of mixed-dimensional perovskite films[34,35].

The properties of MHPs for PL-type displays and of PeLEDs for EL-type displays are summarized in TABLE 1. Stability against air, moisture and ultraviolet irradiation can be obtained by encapsulation[36–39].

Colour-conversion films based on perovskite nanocrystals (PeNCs) have been developed by various companies (such as Quantum Solutions, Avantama, Peroled, Nanolumi, Zhijing Nanotech and Helio Display Materials). At present, PeNC colour-conversion layers retain more than 70–80% of the initial PL (such as QDot LCD SharpGreen perovskite film) after more than 1,000 hours under heat (85 °C) and high humidity (90% relative humidity at 60 °C).

Green-emitting and red-emitting PeLEDs have EQE of over 20% (green: 23.4% at 531 nm (REF.[6]), red: 23% at 640 nm (REF.[3])), exceeding the EQE of fluorescent OLEDs, but the highest efficiency of blue-emitting PeLEDs is just 12.3% at 479 nm (REF.[7]). Further improvements in device engineering and light outcoupling are needed for high-efficiency PeLEDs to reach their theoretical EQE, which is about 30% for PeNC LEDs[6].

The operational lifetime of PeLEDs does not yet meet the requirement for commercial use (half-lifetime (T_{50}) > 10,000–400,000 hours at 1,000 cd m^{-2}), which varies depending on the emission colour and application[40,41]. The lifetime of PeLEDs has improved less quickly than has their efficiency (FIG. 1a). The longest T_{50} for PeLEDs is 250 hours (at 100 cd m^{-2}) for green[42], 2,100 hours (at 100 cd m^{-2}) for red[43], and <12 hours (at 102 cd m^{-2}) for blue[44]. It is difficult to make a fair comparison with vacuum-deposited OLEDs because PeLEDs are made by solution processing, but it is clear that the operational lifetime of PeLEDs is still poor for practical applications.

To enable the application of PeLEDs in high-colour-purity displays that satisfy Rec.2020, four requirements must be met: emission wavelength (630 nm for red, 532 nm for green and 465 nm for blue), colour purity (FWHM < 30 nm for red, <20 nm for green and blue), high device efficiency and long lifetime.

The colour gamut of organic emitters, Cd QDs, Cd-free QDs, PeNCs and polycrystalline perovskites are compared in FIG. 1b. A narrow FWHM and appropriate emission wavelength determine the coverage of Rec.2020. The large FWHM (>40 nm) of organic emitters covers only a small portion of Rec.2020 (REFS.[45–47]). Several narrowband OLEDs have been reported, but their Rec.2020 agreement is lower than that of PeLEDs owing to a broader shoulder peak and tail[48,49]. QDs have FWHMs between 20 nm and 40 nm, but owing to their nonideal size and distribution control, their Rec.2020 agreement is lower than that of MHPs[50–52]. By contrast, the FWHM and emission colour of MHPs are not strongly dependent on their size[53]. PeNCs and polycrystalline MHPs cover about 100% of the Rec.2020 area[9,54,55] (FIG. 1c).

Synthesizing organic emitters takes several days, the longest production time among emitters[56–58] (FIG. 1d). The production time of QDs is estimated to be around 6 hours considering the slow reaction and shell-growing steps[59,60]. Perovskites require the shortest production time. Ligand-assisted reprecipitation takes around 10 minutes per reaction[61,62], and hot injection takes around 1 hour, including precursor preparation and reaction time[6,11].

We evaluate material cost according to the price of precursors. Perovskites are composed of inexpensive materials (such as $CsPbBr_3$, requiring $PbBr_2$ and Cs_2CO_3, at an average cost of US$2 per gram)[11] compared to Cd QDs (such as CdSe/ZnS, requiring $Cd(OAc)_2$, ZnO, Se, S and OA, at an average cost of US$5 per gram)[59], Cd-free QDs (such as InP/ZnSe/ZnS, requiring $In(C_2H_3O_2)_3$, $[(CH_3)_3Si]_3P$, $Zn(OAc)_2$, Se and S, at an average cost

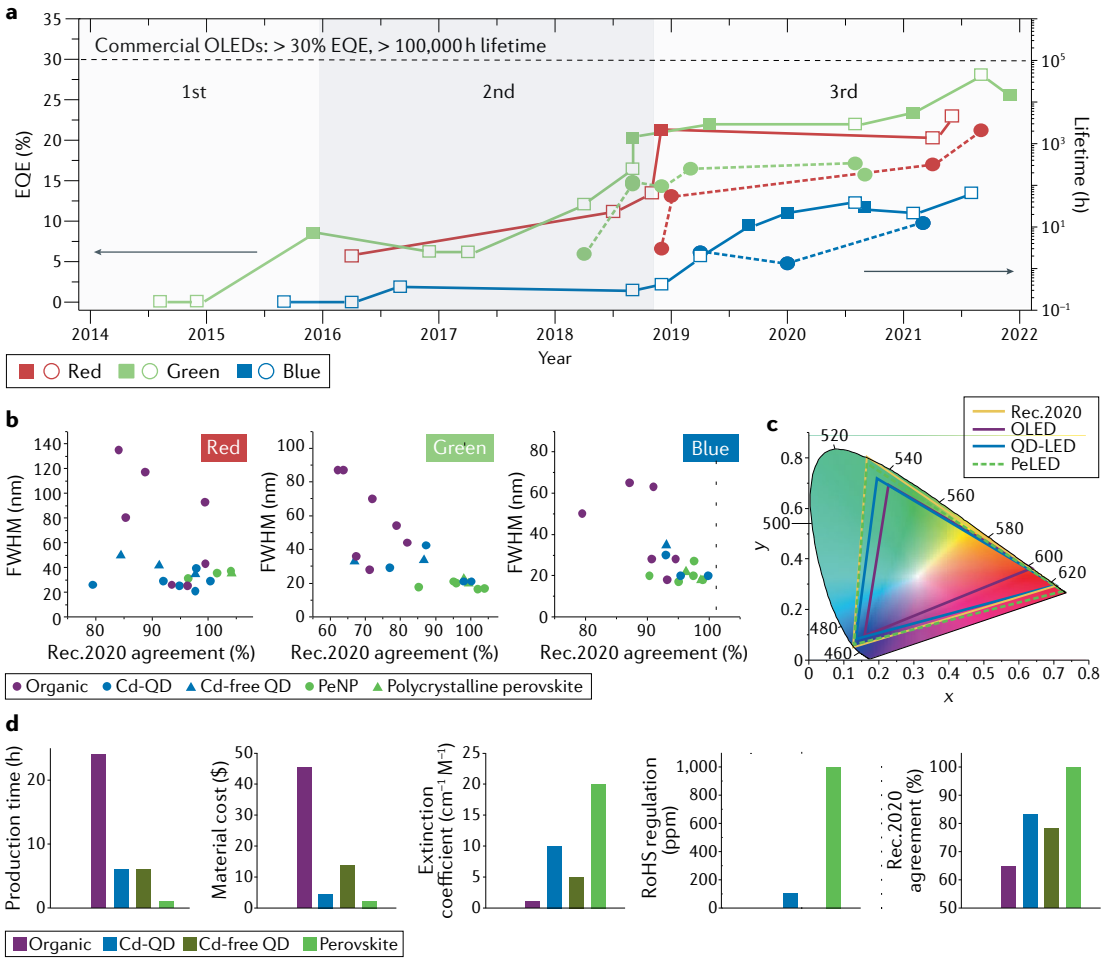

Fig. 1 | **Current status of perovskite light emitters. a** | Evolution over time of the external quantum efficiency (EQE) and the lifetime of perovskite light-emitting diodes (PeLEDs). The values for commercial organic light-emitting diodes (OLEDs) are marked for comparison. Filled squares indicate the EQE values obtained considering the full angular EL distribution and hollow squares indicate the EQE values calculated using the Lambertian assumption. If the PeLED is treated as a Lambertian source, the radiance is independent of viewing angle, and the EQE calculation can be simplified using a single measurement at a viewing point parallel to the pixel. However, the Lambertian assumption leads to errors when the light source has non-Lambertian emission, and the radiance depends on the viewing angle. Because PeLEDs, unlike OLEDs, tend to have non-Lambertian emission, full angular measurements are required to obtain accurate EQE values[201]. Circles indicate the electroluminescence lifetime for each colour. **b** | Rec.2020 agreement and full width at half maximum (FWHM) for red, green and blue for different classes of emitters. The Rec.2020 agreement represents the percentage of the colour gamut encompassed by two primary colours of Rec.2020 and one colour of the light emitter, compared to that covered by the three primary colours of Rec.2020. **c** | Colour gamut coverage of displays made of different materials. The CIE chromaticity diagram and the colour gamut coverage of OLEDs, quantum dot LEDs (QD-LEDs) and PeLED were obtained from published data. PeLED: red (wavelength 689 nm, FWHM 35.6 nm)[65], green (wavelength 529 nm, FWHM 22.8 nm)[54], blue (wavelength 466 nm, FWHM 17.9 nm)[9]; QD-LED: red (wavelength 640 nm, FWHM 29 nm)[232], green (wavelength 535 nm, FWHM 42 nm)[52], blue (wavelength 464 nm, FWHM 20 nm)[233]; OLED: red (wavelength 644 nm, FWHM 117 nm)[233], green (wavelength 520 nm, FWHM 44 nm)[234], blue (wavelength 425 nm, FWHM 63 nm)[46]. **d** | Comparison of light-emitting materials from economic and environmental viewpoints. Material cost is in US dollars in 2020. ppm, parts per million; RoHS, Restriction of Hazardous Substances.

of US$14 per gram)[63] and the organic emitter $Ir(ppy)_3$ (about US$45 per gram)[58].

The extinction coefficient k of a material is related to its ability to absorb light. Perovskites have a higher k (20–50 (cm μM)$^{-1}$) than Cd QDs (2–8 (cm μM)$^{-1}$), Cd-free QDs (1–5 (cm μM)$^{-1}$) and organic emitters (0.01–1 (cm μM)$^{-1}$)[64–67]. Therefore, colour-conversion layers based on perovskites require less material.

The Restriction of Hazardous Substances (RoHS) directive limits the concentration of hazardous substances to ≤100 ppm for Cd and ≤1,000 ppm for Pb by weight[68]. Hence, Cd QDs are more strictly regulated than MHPs. Organic emitters and Cd-free QDs are not restricted by RoHS.

New opportunities for perovskite emitters

The use of displays has been extended to include applications such as LED walls and digital signage, and the advent of the internet of things positioned displays as a medium of visual interaction between humans and the

Table 1 | **Performance of state-of-the-art MHPs for PL and EL applications**

MHP composition	Strategy	Ligand or passivation agent	Performance (PLQY for PL and EQE for EL applications)	Stability	Wavelength (nm)	FWHM (nm)	Year	Ref.
PL applications								
$CsPbBr_3$	Oxides core–shell	SiO_2	71%	Over 50 days in H_2O, HCl, ultraviolet irradiation	–	20	2020	36
$MAPbBr_3$	Oxides core–shell	SiO_2	70%	Over 600 days in H_2O, O_2, HCl and NaOH solution	530	22	2021	23
$MAPbBr_3$	Oxides core–shell Organic core–shell	SiO_2 and PVDF	85.5%	Over 30 days in H_2O, over 60 days in air	530	27	2019	222
$CsPbBr_3$	Organic core–shell	PS-2-PVDF	51%	Over 60 days in EtOH/IPA	–	23	2017	133
$FAPbBr_3$	Organic passivation	SEBS	82%	Over 70 days in H_2O	522	–	2020	70
$CsPbBr_3$	Perovskite core–shell	Cs_4PbBr_6	96.2%	Over 7 days in air	516	–	2018	223
$CsPbBr_3$	Perovskite core–shell	Rb_4PbBr_6	85%	Over 2 days in ultraviolet irradiation	505	–	2018	224
EL applications (nanocrystals)								
$CsPbBr_3$	Ligand engineering	NaBr	~12.3%[a]	20 h at 90 cd m^{-2}	479	–	2020	7
$FAPbBr_3$	Ligand engineering	2-Naphthalene sulfonic acid	~19.5%[a]	20 min at 100 cd m^{-2}	532	21	2021	225
$CsPbBr_3$	Ligand engineering	NaBr	~22%[a]	1 h at 1,200 cd m^{-2}	504	–	2020	7
$CsPbBr_3$	Ligand engineering	$ZnBr_2$	~16.48%[a]	136 min at 0.6 mA cm^{-2}	518	18	2018	99
$CsPbI_3$	Ligand engineering	KI	~23%[a]	10 h at 200 cd m^{-2}	640	31	2021	3
$CsPb(Br/I)_3$	Ligand engineering	OLA-HI	21.3%	5 min at 100 cd m^{-2}	649	31	2018	4
		An-HI	14.1%	180 min at 100 cd m^{-2}	649	29	2018	4
$CsPbBr_3$	Ligand engineering	DDDAM/PEA	~4.7%[a]	12 h at 102 cd m^{-2}	470	27	2021	44
	Defect passivation	HBr etching	~4.7%[a]	12 h at 102 cd m^{-2}	470	27	2021	44
$FA_{0.9}GA_{0.1}PbBr_3$	Defect passivation	GABr, TBTB	23.4%	132 min at 100 cd m^{-2}	531	–	2021	6
$CsPbI_3$	Defect passivation	PMA	~17.8%[a]	317 h at 30 mA cm^{-2}	689	37	2021	5
$FAPbBr_3$	Interfacial engineering	TBB	~20.1%[a]	2.9 h at 100 cd m^{-2}	531	20	2020	8
$CsPbBr_3$	Interfacial engineering	TSPO1	~18.7%	15.8 h at 100 cd m^{-2}	516	20	2020	197
$CsPbBr_3$	Device structure engineering	PO-T2T/TPBi	21.63%	180.1 h at 100 cd m^{-2}	520	18	2021	119
EL applications (polycrystalline thin films)								
$(Rb/Cs/FA)Pb(Br/Cl)_3$	Vapour-assisted crystallization/defect passivation	Ru^+	~11.0/ 5.5%[a]	~1–2 min	477/ 466	18	2021	10
CsPbBr3/MABr	Defect passivation	MABr	~20.3%[a]	10.42 min at 7,130 cd m^{-2}	525	20	2018	32
$FA_{0.33}Cs_{0.67}Pb(I_{0.7}Br_{0.3})_3$	Defect passivation	FPMATFA	~20.9%[a]	14 h at 2.5 mA cm^{-2}	694	37	2021	226
$PEA_2Cs_{n-1}Pb_nX_{3n+1}$	Defect passivation	18-Crown-6, poly(ethylene glycol) methyl ether acrylate	~28.1%[a]	4.04 h at 100 cd m^{-2}	–	–	2021	227
FPMAI: $MAPbI_3$	2D–3D mixed MHP/ blade coating	–	~16.1%[a]	19.6 h at 3 mA cm^{-2}	725	–	2021	228
$PEA_2Cs_{1.6}MA_{0.4}Pb_3Br_{10}$	2D–3D mixed MHP/ defect passivation	Tris(4-fluorophenyl) phosphine oxide	25.6%	115 min at 7,200 cd m^{-2}	517	50	2021	229

Table 1 (cont.) | **Performance of state-of-the-art MHPs for PL and EL applications**

MHP composition	Strategy	Ligand or passivation agent	Performance (PLQY for PL and EQE for EL applications)	Stability	Wavelength (nm)	FWHM (nm)	Year	Ref.
EL applications (polycrystalline thin films) (cont.)								
$CsPbBr_3$:PEACl	2D–3D mixed MHP/ defect passivation	YCl_3	11.0/ 4.8%	–	485/477	–	2019	178
p-$FPEA_2MA_{n-1}Pb_nBr_{3n+1}$	2D–3D mixed MHP/ defect passivation	CF_3KO_3S	20.36%	6.5 min at 10,000 cd m^{-2}	~525	20.1	2021	230
$PEA_2PbBr_4(CsPbBr_3)_4$	2D–3D mixed MHP/ defect passivation	Ethoxylated trimethylolpropane triacrylate	~22.49%[a]	52 min at 144 cd m^{-2}	508	20	2021	213
PEABr: $CsPbBr_3$	2D–3D mixed MHP/ crosslinking/defect passivation	Methylene-bis-acrylamide, $K_2S_2O_8$	16.8%	208 h at 100 cd m^{-2}	516	17	2021	140
$CsPbBr_3$	Crystal size reduction/ defect passivation	Cs-TFA	~10.5%[a]	250 h at 100 cd m^{-2}	518	19	2019	42
PBABr: (Cs/FA)$PbBr_3$	In situ nanocrystal formation	–	9.5%	250 s at 100 cd m^{-2}	483	26	2019	165
$PEA_2Cs_{n-1}Pb_n(I_{0.6}Br_{0.4})_{3n+1}$	In situ nanocrystal formation	Perovskite matrix	~18%[a]	25 h at 914 cd m^{-2} 2,100 h at 100 cd m^{-2}	650	–	2021	43
PEACl:$CsPbBr_3$	Device structure engineering	Conjugated polyelectrolytes TB(MA)	~13.5%[a]	290 s at 5 V	488	–	2021	231

An-HI, aniline hydroiodide; Cs-TFA, caesium trifluoroacetate; DDDAM, didodecylamine; EL, electroluminescence; EQE, external quantum efficiency; EtOH, ethanol; FPMAI, fluorophenylmethylammonium iodide; FPMATFA, 4-fluorophenylmethylammonium-trifluoroacetate; FWHM, full width at half maximum; GABr, guanidinium bromide; IPA, 2-propanol; KI, potassium iodide; MHP, metal halide perovskite; OLA-HI, oleylammonium hydroiodide; PBABr, phenylbutylammonium bromide; PEA, phenethylamine; PEABr, phenethylammonium bromide; *p*-FPEA, *p*-fluorophenethylamine; PL, photoluminescence; PLQY, photoluminescent quantum yield; PMA, poly(maleicanhydride-alt-1-octadecene); PO-T2T, 2,4,6-tris[3-(diphenylphosphinyl)phenyl]-1,3,5-triazine; PS, polystyrene; PVDF, polyvinylidene fluoride; SEBS, styrene-ethylene-butylene-styrene; TBB, 1,3,5-tris(bromomethyl) benzene; TB(MA), conjugated polyelectrolyte with $CH_3NH_3^+$ (MA^+) counterion; TBTB, 1,3,5-tris(bromomethyl)-2,4,6-triethylbenzene; TPBi, 2,2′,2′′-(1,3,5-benzinetriyl)-tris(1-phenyl-1-H-benzimidazole); TSPO1, oxide-4-(triphenylsilyl)phenyl.
[a]EQE calculated with Lambertian assumption.

internet[69]. LCDs and LEDs are the two main types of displays, and MHPs can be applied in both. In LCD screens, MHPs can be used as a colour-conversion layer that downshifts the backlight to yield RGB light[70,71] (FIG.2a, left). TCL and Zhijin Nanotech have demonstrated commercial LCD televisions based on perovskite-QD films. MHPs can also be used as EL-type LEDs and form the light-emitting component in the display[6] (FIG. 2a, right).

Near-eye displays are a newly emerging hardware format to realize augmented and virtual reality (AR and VR). Considering the distance between the eyes and the display, a near-eye display requires a very high resolution (>6,000 pixels per inch) to prevent a pixelated view[72]. Therefore, a delicate patterning process must be developed to reduce pixel size and pitch[73]. Also, the conventional colour-conversion layers based on QDs must be thick enough to achieve high colour conversion efficiency[74], and a thickness of more than 5 μm is required (usually 50–100 μm free-standing QD enhancement films are used for televisions)[75]. This requirement prevents the application of QD colour-conversion layers in near-eye displays with a thin profile. As MHPs have a high extinction coefficient, a colour-conversion layer based on MHPs can effectively absorb the backlight with thicknesses smaller than 5 μm (REFS.[64–67]). The reduced thickness of the colour-conversion layer enables a high-resolution patterning process[76].

Finally, LED lighting with high efficiency and long lifetime has replaced incandescent and fluorescent lamps in the market[77]. The colour-tuneable emission with narrow FWHM of PeLEDs can be used for sophisticated special lighting tasks. For example, red and blue lighting can be used in greenhouses to stimulate the growth and development of plants[78]. Colour-tuneable lighting could be used for human-centric lightings, as different colour temperatures influence hormonal secretion and biological rhythms[79].

Technical challenges and roadmap

The technical roadmap for the development of perovskite light emitters over the next 10 years is shown in FIG. 2b, and is determined by the timeline of potential market entry. The potential markets are categorized by applications such as PL-type and EL-type displays, general and special lighting, and AR and VR. The timelines for the markets, industrial demands and technical developments indicate the expected time at which each application will enter the market, detemined by comparing the technical maturity of the required materials and devices to the concomitant industrial requirements for each application, and the time needed to develop processes and technologies for the production of materials and devices. PL-type displays are considered an application in which MHPs could be used within 4 years. AR and VR displays are expected to be the last application to be realized (Supplementary information).

To apply MHPs at the industrial level, PeLEDs must both meet Rec.2020 requirements and achieve

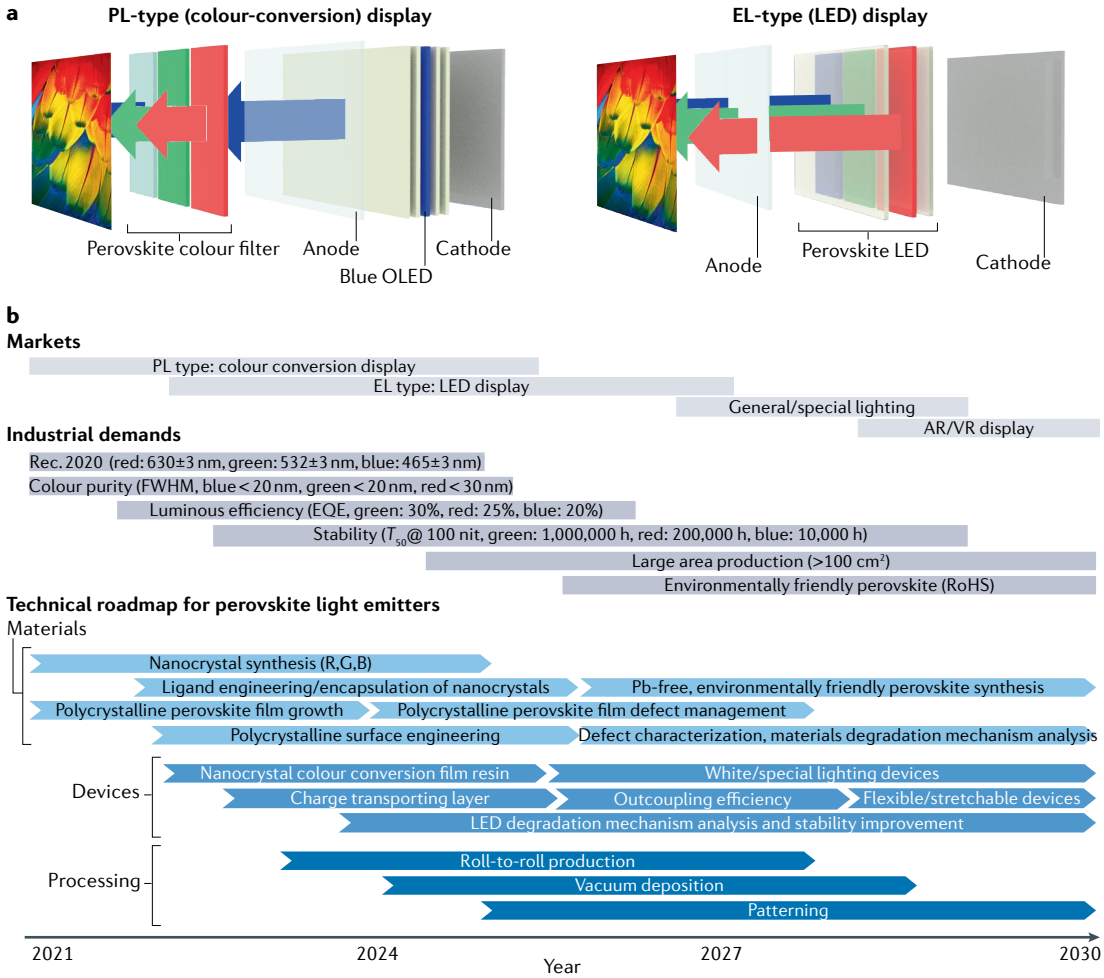

Fig. 2 | **Technical roadmap for perovskite light emitters. a** | Metal halide perovskites can be used as colour-conversion layers in photoluminescence (PL)-type displays (left) or as light emitters in electroluminescence (EL)-type light-emitting diode (LED) displays (right). **b** | Technical roadmap for the development of perovskite-based light emitters and light-emitting diodes over the next 10 years. AR/VR, augmented and virtual reality; EQE, external quantum efficiency; FWHM, full width at half maximum; Nit, candela per square metre; OLED, organic light-emitting diode; RoHS, Restriction of Hazardous Substances. Multi-colour images in panels **a** and **b** credit: THEPALMER/Getty Images.

high environmental stability. The primary colours of Rec.2020 are equivalent to monochromatic light sources, so the 100% colour gamut of Rec.2020 cannot possibly be met by PeLEDs, because the colours of PeLEDs are limited by the bandgap tuneability and by the slightly broad FWHM. Instead, wavelengths for primary colours (630 nm for red, 532 nm for green and 465 nm for blue) and narrow FWHMs (<30 nm for red, <20 nm for green and blue) were set as the first practical goal, leading to an approximately 96% coverage of the Rec.2020 colour gamut.

Target luminescence efficiencies and operational lifetimes for each colour are specified in FIG. 2b for EL-type display applications, which are expected to be developed within 6 years, based on the timing of the development of OLED displays. Prime requirements are the ability to produce large-area MHP emitter films or PeLEDs for large-area displays and lighting applications, and to develop environmentally benign MHP compositions that meet the RoHS requirements (Supplementary information). Following the technical roadmap presented here, we discuss the research challenges that must be resolved to enable successful industrial applications, and identify some technologies that need to be developed to address these challenges. The purpose of this Review is to provide researchers with a clear direction for the technological evolution of MHPs for practical display and lighting applications.

Perovskite nanocrystals

PeNCs are colloidal nanocrystals about 10 nm in size surrounded by organic ligands with a low dielectric constant that effectively confine excitons in the PeNCs and promote radiative recombination[80]. The emission colour of PeNCs with sizes larger than the exciton Bohr diameter does not depend strongly on size. Therefore, line broadening caused by size inhomogeneities is negligible and a narrow FWHM can be achieved[53,81].

PeNCs are expected to be the first MHPs to find application in PL-type displays thanks to their high PLQY and scalable processability[82,83]. However, owing to their high surface-to-volume ratio and unstable ligands,

PeNCs easily agglomerate, which reduces their PLQY. Therefore, the chemical dynamics of PeNC surface and ligands must be better understood, and methods to suppress surface defects must be developed. Also, EL-type displays require efficient charge injection, and so the electrical properties of PeNCs must be considered[81]. Strategies such as ligand engineering, composition engineering and defect passivation have been introduced to achieve a high EQE in PeNC PeLEDs (FIG. 3a).

In this section, we discuss the application of defect engineering, surface chemistry and ligand engineering in PeNCs. Additionally, we introduce the use of core–shell structures to overcome the poor stability of PeNCs.

Perovskite nanocrystal synthesis. Various approaches can be used to synthesize PeNCs[8,84,85]; the main ones are ligand-assisted reprecipitation[61,62] and hot injection[11]. Room-temperature triple ligand synthesis[84], ultrasonication[8,85], grinding and high-temperature solid-state synthesis[86] are other methods used to synthesize PeNCs. Ligand-assisted reprecipitation is a good option for achieving fast and cost-effective synthesis for commercialization, because the reaction takes only a few minutes in ambient conditions at room temperature[61,62]. Longer amine ligands and larger amounts of oleic acid (OA) lead to smaller PeNCs[53,87] (FIG. 3b). However, ligand-assisted reprecipitation results in low PLQY and has low production capacity. I^- in red PeNCs strongly interacts with polar solvents and bonds weakly with ligands[88,89]; Cl^- in blue PeNCs introduces deep trap states and has low solubility[90]. Using less coordinative polar solvents such as gamma-butyrolacton or acetonitrile can improve the PLQY and stability of red PeNCs[91], and introducing soluble Cl-based precursors in nonpolar solvents should improve the PLQY and production capacity of blue PeNCs[92–94].

In the hot injection method, Cs-oleate is injected into a PbX_2 solution at a certain reaction temperature. Then, the precursors thermally decompose and recrystallize as PeNCs[11]. The shapes, sizes and phases of the PeNCs can be controlled by adjusting the temperature, ligands and precursors. Higher reaction temperatures yield larger PeNCs. Nanoplatelets or nanorods can also be fabricated at low temperature with high Cs/Pb ratios[95,96] (FIG. 3c). The hot injection method requires a high temperature of 170–200 °C, complicated precursor preparation and inert conditions. Moreover, the method requires fast quenching.

To obtain PeLEDs with high efficiency and long lifetimes, high PLQY and facile charge injection are required. Regardless of synthesis methods, PeNCs show n-type properties that include a deep VBM and a Fermi energy close to the CBM[95,97–102], which hinder hole injection and cause charge imbalance. These issues are possibly caused by halide vacancies, which lead to non-radiative recombination and n-type defects[103–105], and metallic Pb^0 generated on the surface of MHPs, which induces Fermi-level pinning at the CBM and contributes to the n-type characteristics[106].

Modulating the precursors and additives during synthesis can increase the PLQY and facilitate charge injection. Introducing large amounts of metal dihalides, MX_2, as an additive during the synthesis of PeNCs leads to halide-rich conditions and prevents the formation of halide vacancies. Alternatively, metal cations can either be doped into the lattice or located at the surface to stabilize or passivate the PeNCs[107–112]. For example, CuI_2 or ZnI_2 doping yields a stable α-phase, high PLQY (>90%) and increased EQE[96,101]. Zr^{4+} modifies the surface of $CsPbI_3$ and prevents the formation of Pb^0 (REF.[100]). The energy level shift results in a lower hole injection barrier, yielding high luminance and limited decrease in efficiency with increasing brightness[100]. Additionally, surface passivation using Zn^{2+}, K^+ and Nb^{3+} can upshift the band edge of PeNCs and increase the EQE[99,101,102] (FIG. 3d). When using ligand-assisted reprecipitation, tuning the ratio of FABr to $PbBr_2$ can modulate the electrical transport of $FAPbBr_3$ nanocrystals. The shallowest VBM (about 5.85 eV) at the optimized ratio of 2.2:1 resulted in a maximum EQE of 17.1%, and a maximum luminance of 67,115 cd m^{-2} (REF.[100]).

Ligand engineering of perovskite nanocrystals. PeNCs have a high surface-to-volume ratio and low defect-formation energy at the surface[113]. Therefore, understanding their surface chemistry and the interactions between ligands and MHPs is a short-term goal that will help to achieve high efficiency and stability.

The instability of PeNCs is attributed to three reasons. First, acid-base reactions between OA and oleylamine (OLA) reversibly detach them from the surface, leaving an under-coordinated surface[114]. Second, chemical reactions between OLA and OA to form oleyl oleamide cause surface defects and agglomeration of PeNCs[115,116]. The oleyl oleamide reaction also generates H_2O that can damage the perovskite[37]. Third, OLA can coordinate with adjacent surface X^- and readily detach from the surface in the form of oleylammonium halide[114].

Moreover, the insulating long-chain ligands limit the efficiency of PeLEDs. A highly conductive PeNC layer is required for efficient charge injection to obtain high luminance and stability. Also, a reduction in the series resistance in devices reduces Joule heating, and therefore prevents thermal degradation of the perovskite[3]. Furthermore, high conductivity reduces local carrier concentration, thus suppressing Auger recombination[117].

The main strategies for ligand engineering are washing, post-treatment (or ligand exchange) with shorter ligands or halide compounds, and using tightly binding ligands.

The washing strategy effectively decreases the ligand density, thus increasing charge injection into PeNCs[118–120]. Additionally, washing removes more OA than OLA, suppressing the acid–base reactions and increasing the colloidal stability[115]. Methyl acetate, ethyl acetate and acetone are used as flocculation solvents[120,121].

The washing process inevitably decreases the PLQY because the removal of ligands generates surface defects[120,122]. Therefore, additional ligands of halide anions are added (the ligand exchange strategy) into the washed PeNCs to passivate trap sites[7,117,120]. Moreover, halide anions have a higher affinity than oleate does to Pb^{2+}, so they remove the remaining OA and prevent further acid–base reactions[4,44,123]. Post-treatment

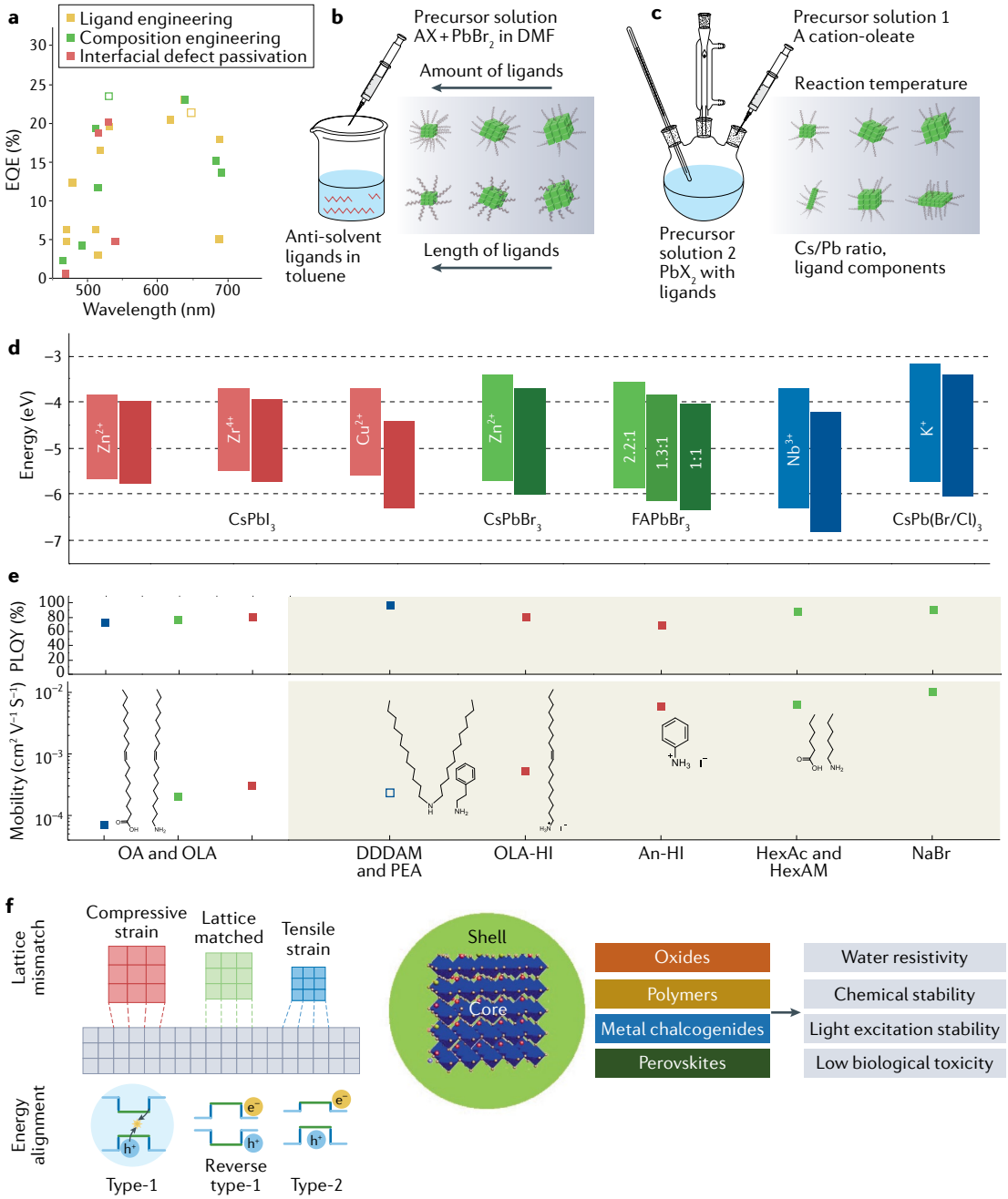

using oleylammonium iodide (OLA-HI) or aniline hydroiodide (An-HI) has enabled a high EQE (20.3%) in red PeLEDs[4]. Didodecyldimethylammonium bromide (DDAB) has been widely used as a stable ligand to replace OA and OLA. Fully substituted quaternary amines are permanently charged, and therefore are not neutralized by the acid–base reaction. Moreover, Br^- in DDAB passivates the surface of the PeNC[123]. A bipolar shell consisting of an X^- inner shell and an A^+ cation (NaBr[7]/KI[3]) outer shell yielded an EQE of 23% for red[3] and of 12.3% for blue[7]. The bipolar shell provides colloidal stability by electrostatic repulsion without insulating ligands, thus imparting high hole mobility (10^{-2} cm^2 V s^{-1}) to PeNCs[7].

In the tightly binding ligands strategy, to prevent ligand detachment, strongly bound ligands are used. For example, bidentate ligands[124] or zwitterionic ligands[125] bind stably to the PeNC surface because of additional binding groups and chelating effects. In addition, softer acids such as phosphonic acid[126,127] and sulfonic acid[128,129] have been introduced to strongly bind to uncoordinated Pb, according to soft–hard acid–base theory[90].

Ligands can affect the hole and electron mobility of PeNCs[95,97–102] (FIG. 3e). Ligand-exchanged PeNCs show high mobility and a high PLQY, and can thus be suitable for both PL and EL applications. PeNCs coated with OA and OLA have high PLQY, comparable to that of ligand-exchanged PeNCs produced using compositional engineering followed by an adequate washing process[95]. However, the carrier mobility of PeNCs coated in OA and OLA is low, limiting EL efficiencies.

Fig. 3 | **Synthesis and surface-modification strategies for PeNCs. a** | External quantum efficiency (EQE) versus wavelength obtained with different strategies to engineer perovskite nanocrystals (PeNCs) for perovskite light-emitting diodes (PeLEDs). Filled squares indicate EQEs calculated with the Lambertian assumption; hollow squares indicate EQEs calculated considering the full angular emission. **b** | Ligand-assisted reprecipitation method for the synthesis of PeNCs. **c** | Hot injection method for the synthesis of PeNCs. **d** | Energy-level diagrams of various PeNCs. Both the conduction band minimum (CBM) and the valence band maximum (VBM) shift up after doping and surface passivation (with Zn^{2+}, Zr^{4+}, Cu^{2+}, Nb^{3+} or K^{+}), or adjusting the FABr:$PbBr_2$ ratio to 2.2:1. The upshifted bands (left, pristine bands are the ones on the right) reduce the hole injection barrier and enhance hole injection. **e** | Photoluminescence quantum yield (PLQY) and carrier mobility of PeNCs with different ligand composition. The mobility values are derived from the space charge limited current of hole-only and electron-only devices. The filled squares indicate hole mobility, the hollow square indicates electron mobility. The colour of each point represents the emission colour of the corresponding PeNC. The shading highlights the ligands that could be alternatives to the traditional oleic acid (OA) and oleylamine (OLA). **f** | Requirements, examples and positive effects of the core–shell structure of PeNCs. The lattice parameters of the core and shell should be similar. If there is a substantial lattice mismatch, both core and shell are under compressive or tensile strain, which causes high defect density and rough shell morphology. Type-1 energy alignment (deeper VBM and shallower CBM for the shell) is preferable for core–shell structures that confine excitons in the core. Alignment of reverse type-1 (shallower VBM and deeper CBM for the shell) or type-2 (both the VBM and CBM are deeper for the shell, or vice versa) cannot confine excitons in the core. Various kinds of material (such as oxides, polymers, metal chalcogenides and perovskites) can be used for shells. An-HI, aniline hydroiodide; DDDAM, didodecylamine; DMF, dimethylformamide; OLA-HI, oleylammonium hydroiodide; PEA, phenethylamine. Data plotted in panel **d** is from REFS.[95,97–102]; data plotted in panel **e** is from REFS.[4,7,44,95,235].

Core–shell perovskite nanocrystals. Considering the outstanding PLQY but poor material stability of PeNCs, increasing their stability will be the main task for the next 5 years (FIG. 2b). To this end, core–shell structures and encapsulated PeNCs have been developed.

For PL-type displays, various insulating shell materials and encapsulating polymers have been introduced to increase the stability against oxygen, moisture and light, or to reduce the toxicity of PeNCs for use in colour-conversion layers (FIG. 3f). Core–shell structures that use inorganic oxides (SiO_2, AlO_x, TiO_2) give high stability to PeNCs by protecting them from water[130–135]. In particular, densely packed shell structures have excellent chemical stability and reduced toxicity. SiO_2 shells organized by crosslinking were shown to protect the perovskite from oxygen, water, acid or base solutions for 600 days[37]. Cells could proliferate on core–shell PeNCs, proving their biocompatibility and decreased toxicity[37]. A green colour-conversion layer with crosslinked $MAPbBr_3$ showed 89% of Rec.2020 coverage, and a white-emitting colour-conversion layer LED with crosslinked $MAPbBr_3$ and red-emitting Cd QDs maintained CIE coordinates (0.316, 0.318) for 400 days[37].

Embedding PeNCs in a polymer matrix is another way to protect them from air and moisture, as long as the polymer has high affinity with the PeNC ligands[136]. Styrene–ethylene–butylene–styrene with high compatibility with PeNCs suppressed PeNC degradation in water for 70 days[70].

For EL-type displays, the stability and lifetime of PeNCs have increased continuously: a T_{50} of several hundreds of hours at 100 cd m^{-2} was achieved[5,137]. However, this value is still insufficient for commercialization. One of the main reasons for the low lifetime of PeLEDs is ion migration in perovskites[138]. Because 3D–2D structured perovskites[139] and grain-boundary inter-crosslinking[140] can prevent ion migration, forming a core–shell structure is a promising way of increasing the lifetime of PeLEDs. Additional advantages of the core–shell structure are that the shell can passivate surface defects, facilitate exciton recombination[141] and suppress Auger recombination[142].

The synthesis of core–shell PeNCs for EL display must meet several requirements: a type-1 band alignment that confines the excitons in the core and facilitates radiative recombination; a small lattice mismatch between core and shell to prevent traps at the interface[143]; and the use of a semiconducting shell material that does not block charge injection into the core (FIG. 3f). Until now, only a few core–shell PeNCs using alumina[144], metal chalcogenides[145,146] and perovskites[147] as shells have been reported for PeLEDs, and methods to precisely control shell growth and to identify suitable shell materials are needed.

Perovskite polycrystalline thin films

MHP polycrystalline thin films are grown directly from a precursor solution without additional synthetic processes. Such films can be developed as alternative light emitters (instead of PeNCs). Generally, thin-film MHP emitters have a longer operational lifetime in LEDs compared to PeNC PeLEDs because they naturally avoid the problem of surface ligand desorption that occurs in PeNCs (TABLE 1). The absence of surface ligands in thin-film MHP also leads to a higher charge transport capability than in PeNCs. MHP grains are composed of relatively large crystals that are less effective than PeNCs in confining excitons and charges inside the emitter. Also, polycrystalline perovskite thin films inevitably have numerous imperfections at grain boundaries and on the film surface[26,148–150].

According to our roadmap, polycrystalline thin film growth and the passivation of defects inside and on the surface of grains or of the film are critical tasks to be considered first (FIG. 2b). In perovskite polycrystalline thin films, crystal growth is crucial to achieve high crystallinity and the concomitant low trap density. Also, owing to the low binding energy and long carrier diffusion length of MHPs, the grains must be small to ensure spatial charge confinement and limit charge-carrier diffusion, as needed for high-efficiency LED applications[13,24,151]. Therefore, the thin films must have small, carrier-confined perovskite crystals, grown concurrently with passivated grain boundaries and surfaces. The surface morphology of polycrystalline MHP thin films also affects the efficiency and stability of PeLEDs, and should be considered during polycrystalline thin film growth (Supplementary information). PeLEDs fabricated using emitting layers that include polycrystalline thin films have achieved different values of EQE depending on the growth method, such as reduced crystal growth, growth of mixed-dimensional phases, in situ nanocrystal formation and defect passivation (FIG. 4a).

In this section, we summarize the mechanisms of in situ perovskite crystal growth and defect passivation

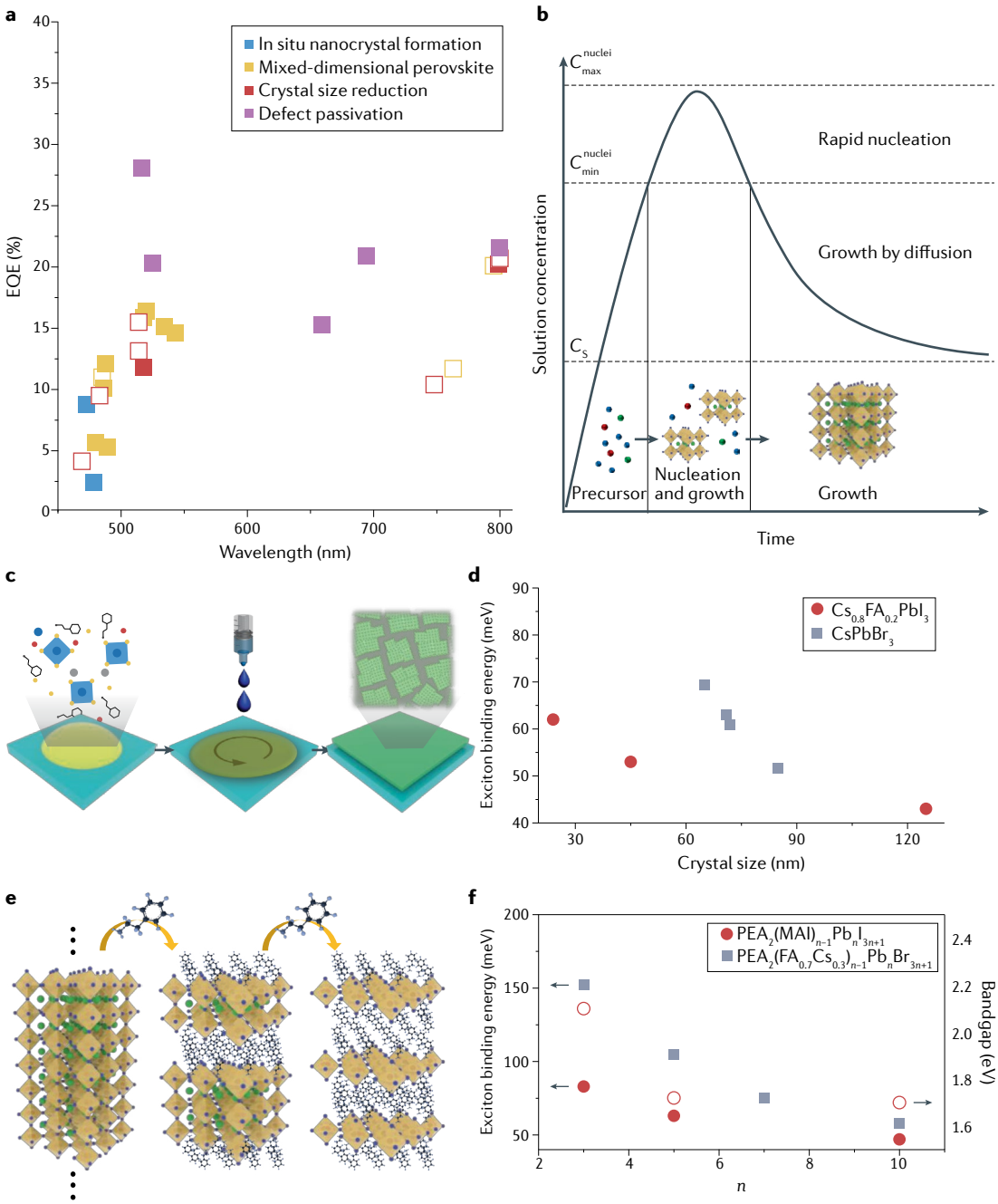

Fig. 4 | **Crystal-growth strategies for perovskite polycrystalline thin films. a** | External quantum efficiency (EQE) versus wavelength obtained with different growth and passivation methods used to obtain polycrystalline perovskite thin films. Filled squares indicate EQEs calculated with the Lambertian assumption; hollow squares indicate EQEs calculated considering the full angular emission. **b** | The LaMer diagram describes changes in precursor concentration in the solution during the crystal growth process. C_s is the critical supersaturation concentration, C_{min}^{nuclei} is the minimum nucleation concentration, and C_{max}^{nuclei} is a critical limiting supersaturation concentration[236]. The mechanism can be divided into three stages: first, there is a sharp increase in free precursor concentration due to solvent evaporation or solubility changes; then, when the solution concentration exceeds C_{min}^{nuclei}, many nuclei form precursor monomers, and this process rapidly reduces the precursor concentration from C_{max}^{nuclei} to C_{min}^{nuclei}; in the final stage, crystal growth is controlled by the diffusion of precursors as long as the monomer concentration exceeds C_s (REF.[237]). **c** | Schematic diagram showing the in situ control of crystal size. The use of an anti-solvent during the spin coating of the precursor solution induces a high nucleation rate and a large number of nuclei, resulting in polycrystalline thin films with small grain sizes. **d** | Exciton binding energy of metal halide perovskites ($Cs_{0.8}FA_{0.2}PbI_3$ and $CsPbBr_3$) as a function of 3D perovskite crystal size. **e** | Schematic diagram showing the formation of layered quasi-2D or 2D perovskites. Mixed-dimensional quasi-2D perovskites generally have the formula $A'_2A_{n-1}B_nX_{3n+1}$, where A′ is a bulky or long-chain organic cation, and *n* is the number of layers of octahedra. **f** | Dependence of the exciton binding energy (full markers) and bandgap (empty markers) on the number of layers in quasi-2D perovskites ($PEA_2(MAI)_{n-1}Pb_nI_{3n+1}$ and $PEA_2(FA_{0.7}Cs_{0.3})_{n-1}Pb_nBr_{3n+1}$). Data for panel **d** is from REFS.[238,239], data for panel **f** is from REFS.[28,162].

strategies for polycrystalline perovskite thin films and their LED applications.

In situ polycrystalline perovskite size control. The nucleation and crystal growth mechanism of MHPs in solution can be explained by the LaMer model (FIG. 4b). The nucleation rate is mostly determined during the nucleation stage, and its control is crucial to determine the size of the final grains and its distribution[152]. At this stage, nucleation occurs only when an activation energy barrier is overcome, so the nucleation rate follows the classical nucleation theory given as $\frac{dN}{dt} = A\exp(-\frac{\Delta G_c}{kT})$ where N is the number of nuclei, A is a constant, ΔG_c is the critical Gibbs free energy, k is the Boltzmann constant, and T is temperature[26]. Therefore, the nucleation rate is also determined by the precursor molecule's intermolecular interactions and by the crystal structure of the MHP[26,148,149].

The use of a volatile anti-solvent during the spin casting of the precursor solution (nanocrystal pinning process) induces a high nucleation rate and the formation of a large number of nuclei, yielding polycrystalline perovskite thin films with small grain sizes, and thereby increasing the PL yield in thin films and the EQE in LEDs[13] (FIG. 4c). Spatial and dielectric confinement methods in small-sized nanograins have been used to achieve charge-carrier confinement in MHPs for PeLEDs. Spatial and dielectric confinement through an additive-based nanocrystal pinning process can be achieved in small crystals by in situ tuning of the nucleation rate and crystal growth rate during solution processing, forming nanograins surrounded by organic additives with a low dielectric constant[13,153]. The light-emitter material's binding energy is closely correlated to the PL and EL quantum yield. The binding energy of MHPs increases as the crystal size is reduced, using in situ strategies to control crystal growth[38,154,155] (FIG. 4d).

The inclusion of an organic semiconductor additive in the anti-solvent further reduces the grain size (50–150 nm) of perovskite crystals owing to increased spatial hindrance, and facilitates charge injection into the MHP[13,153]. The addition of long alkyl-group ammonium halide (n-butylammonium halides) to the precursor solution induces the formation of nanometre-sized layered perovskite grains (about 10 nm) by suppressing 3D perovskite growth, and increases the EQE in PeLED[156]. Organic amino acid additives in the precursor solution control crystal growth to form sub-micrometre-sized faceted perovskite platelets (100–500 nm) with increased radiative recombination and improved light outcoupling due to the concave–convex structured emitting layer, resulting in a high EQE of 20.7%[33].

Mixed-dimensional perovskites. Dimensionality control has been widely used to form 2D layered perovskites (in the Ruddlesden–Popper or Dion–Jacopson phase) and mixed-dimensional phases in perovskite polycrystalline films by incorporating bulky or long-chain organic cations in the 3D perovskite. Mixed-dimensional quasi-2D perovskites generally have the formula $A'_2A_{n-1}B_nX_{3n+1}$, where A′ is a bulky or long-chain organic cation, and n is the number of layers of octahedra in the quasi-2D phase (FIG. 4e). Depending on the structure of large organic cation molecules such as phenylethylammonium halide[28,157,158], 1-naphthylmethyl-amine halide[159–161] or on the relative composition of large organic cations to the perovskite precursors, the number of layers and the crystal structure can be widely tuned in thin films. A small value of n increases the exciton binding energy and the bandgap of the perovskite thin film owing to quantum confinement[162] (FIG. 4f).

In a quantum-confined low-n quasi-2D perovskite phase, the radiative process is caused by excitonic recombination, and the photon energy can be effectively transferred from low-n to larger-n phases, filling traps and thus achieving a high quantum yield[28,163]. The controlled synthesis of structures that work like multiple quantum wells and that are composed of multidimensional phases (layered phases with different number of layers and bandgap) can strengthen the quantum confinement and increase the effective energy transfer rate[159,160]. The combination of a wide-bandgap polymer (poly(2-hydroxyethyl methacrylate, bandgap 4.96 eV) and a quasi-2D–3D mixed-dimensional perovskite showed fast energy transfer to 3D domains within 1 ps, resulting in a high PeLED EQE of 20.1%[25]. Phase distribution in the quasi-2D perovskite film is also critically important[164]. The incorporation of a short-chain α-amino acid (L-norvaline) provided a new crystallization pathway with a lower activation energy, and resulted in an improved energy transfer rate between quasi-2D phases and suppressed phase segregation[162].

In situ perovskite nanocrystal growth incorporating a large amount of bulky or long-chain organic ligands provides a convenient way to achieve highly efficient blue-emitting perovskite polycrystalline thin films. The organic ligands and anti-solvent treatment accelerate in situ ligand-assisted precipitation, leading to the formation of nanosized crystals in the thin films[165,166]. Quantum-confined nanocrystals formed in situ (average size 5.8 nm) embedded in a quasi-2D layered perovskite matrix were used to demonstrate efficient blue PeLEDs (EQE 9.5%, peak wavelength 483 nm); they were obtained by using a large amount of phenylbutylammonium bromide (PBABr) (PBABr:ABr:$PbBr_2$ = 1.1:1:1) and an anti-solvent (ethyl acetate)[165].

The in situ fabrication of nanocrystal films is a promising way of achieving high efficiency and luminance simultaneously, because nanocrystal films have both efficient quantum confinement and good charge transport compared to PeNCs.

Defect management of perovskite emitters

Deep traps (mid-gap states) formation causes charge trapping and provides a non-radiative recombination pathway (luminescence loss), which significantly decreases the luminescent yield and causes material degradation[26,150]. In MHPs, the dominant point defects form shallow traps that do not contribute much to non-radiative recombination[19]. However, because of the ionic nature of charged defects, they migrate under electric fields[167] and can accumulate locally[168] or induce phase segregation[169].

Defects in MHPs can be sorted into three kinds: bulk, surface and interface defects (FIG. 5a). Bulk defects are crystalline defects within the PeNCs or polycrystalline MHPs, and are closely related to the structural stability of crystals. Surface defects are mainly caused by missing atoms or ligands on the surface of PeNCs, at grain boundaries or at the film surface. These defects can be mitigated by ligand engineering or by adding defect-passivating molecules. Interfacial defects occur at the MHP/charge transport layer interface. They cause non-radiative recombination at defective interfaces in devices.

Bulk defects and compositional engineering. The structural stability of MHPs can be predicted using the Goldschmidt tolerance factor ($t = (r_A + r_X)/\sqrt{2(r_B + r_X)}$), where r_A, r_B and r_X are the ionic radii of the monovalent and divalent cations and of the halide anion, respectively[170]. A value of t between 0.8 and 1 generally results in stable perovskites in the cubic or orthorhombic structure. Perovskites with $0.9 \leq t \leq 1$ generally have an ideal cubic structure, whereas $t \geq 1$ means that the A-site is too large, and $t \leq 0.8$ that it is too small, to form stable MHPs. The value of t calculated from the effective ionic radius

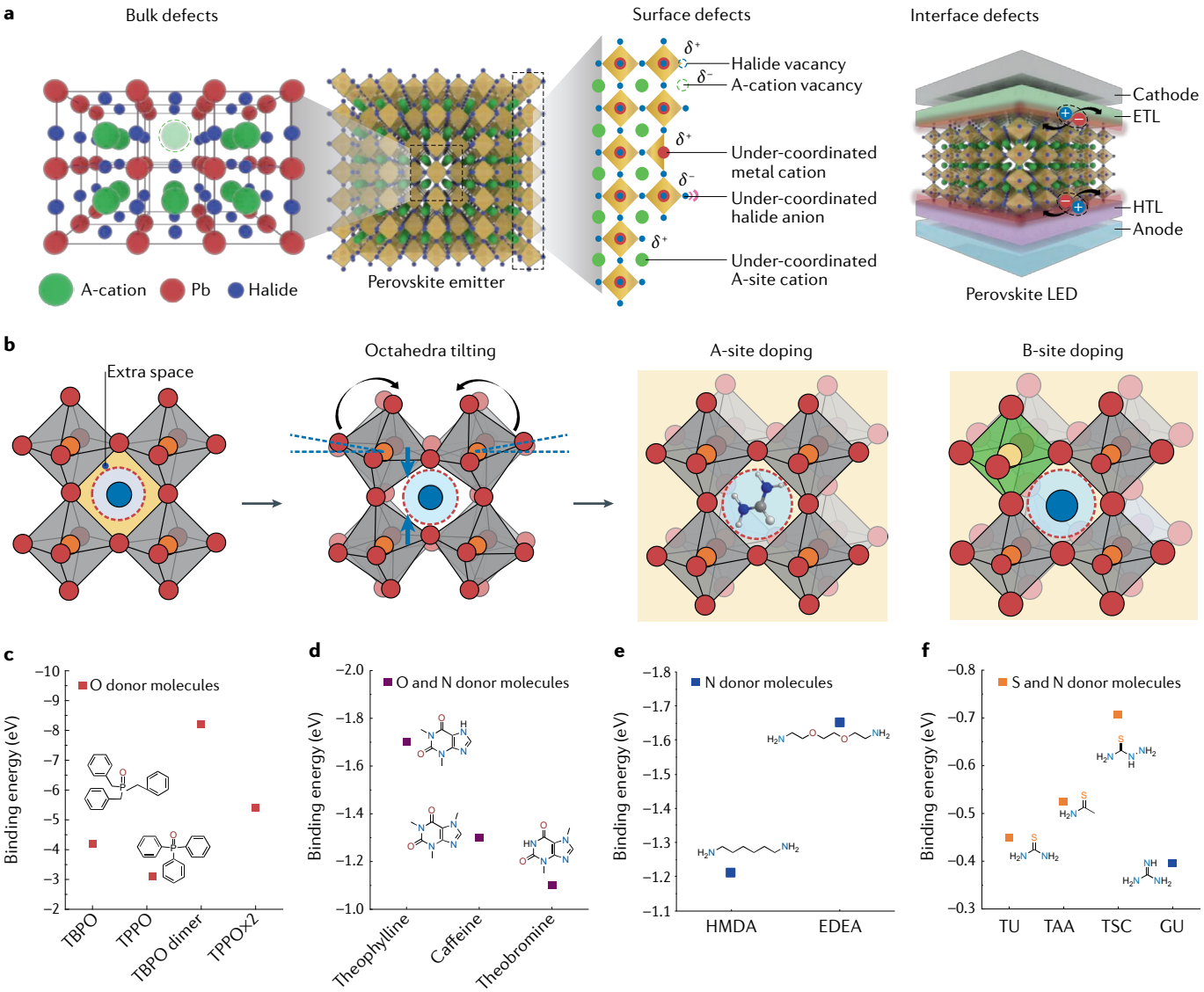

Fig. 5 | **Defect management strategies in perovskites. a** | Schematic showing bulk (an A-cation vacancy as an example), surface and interface defects in metal halide perovskites. **b** | Schematic illustration of the crystal structure and its distortion in perovskites. If the A-site cation is smaller than the space between adjacent $[PbX_6]^{4-}$ octahedra, octahedron tilting occurs to fill the extra space in the A-site, which could be the reason for phase instability. Larger A-site cation (such as FA^+) or smaller B-site cation doping can stabilize the perovskite crystal structure. **c** | Binding energies of tribenzylphosphine oxide (TBPO) and triphenylphosphine oxide (TPPO) on a Pb–I plane perpendicular to the [001] direction, which is the exposed surface of the perovskite crystal. **d** | Binding energies of theophylline, caffeine and theobromine on perovskite surfaces that bear Pb_I antisite defects. **e** | Binding energies of amino-functionalized passivation molecules (hexamethylenediamine (HMDA) and 2,2′-(ethylenedioxy)diethylamine (EDEA)) on a perovskite surface that bears iodine vacancies. **f** | Binding energies of sulfur-containing thiourea (TU), thioacetamide (TAA), thiosemicarbazide (TSC) and a nitrogen donor (guanidine (GU)) on a SnI_2-terminated perovskite surface. Binding energy values cannot be directly compared among panels owing to the use of different calculation methods. ETL, electron-transport layer; HTL, hole-transport layer; LED, light-emitting diode. Data for panel **c** are from REF.[186], data for panel **d** are from REF.[187], data for panel **e** are from REF.[182] and data for panel **f** are from REF.[188].

of Cs^+ (181 pm), MA^+ (270 pm) and FA^+ (279 pm)[171], Cs^+-based MHP ($t \approx 0.8$) show an orthorhombic structure caused by octahedral tilting to fill extra space at the A-site (FIG. 5b). In the case of $CsPbI_3$, the non-emissive orthorhombic δ_O-$CsPbI_3$ phase is energetically more favourable than the emissive cubic α-$CsPbI_3$ phase at room temperature[172,173]. FA^+ perovskites ($t > 1$) have an oversized A-site cation, so the emissive cubic α-$FAPbI_3$ transforms into the non-emissive δ_H-$FAPbI_3$ hexagonal phase[174,175] (FIG. 5b). To stabilize the crystal structure of emissive $CsPbI_3$ and $FAPbI_3$, the mixed A-site cation of (FA/Cs)PbI_3 was introduced to tune t to 1[174]. An entropic stabilization effect due to the mixed composition stabilizes the emissive phase by increasing the free energy of the δ-phase[174,175]. For B-site cations, doping with a small divalent metal halide (MX_2) can improve structural stability by inducing lattice contraction. This alleviation of the distortion of the octahedron yielded stable α-phase $CsPbI_3$[95,98,108,109] (FIG. 5b).

Smaller B-site doping was used to obtain highly efficient and thermally stable $CsPbCl_3$ and $CsPb(Br/Cl)_3$ by increasing the short-range order and reducing halide vacancies[107,111]. Doping with the trivalent metal halide $CeBr_3$ has been investigated, with the goal of improving optical properties, and was found not only to enhance the lattice order by filling the Pb^{2+} and Br^- vacancies, but also to provide additional energy states near the conduction band, which can facilitate radiative recombination[176,177]. Y^{3+} is another trivalent dopant, which can be introduced with a gradient concentrated near the surface. The 4d level of Y^{3+} increases the bandgap of the perovskite, acting as an energy barrier to confine excitons inside grains[178]. Metal halides (such as $ZnBr_2$ in $CsPbBr_3$ (REF.[99]) and KX in $CsPbX_3$ (REFS.[102,179])) also mainly locate at the surface[180]. These metal ions can partially replace the organic ligands, leading to the enhancement of carrier injection and transport efficiency[99,102]. Meanwhile, a surface enriched with K^+ has been proved to increase the binding energy of Br^- and thus to inhibit ion migration[179].

Surface defect passivation. The most common imperfections at grain boundaries or at the surface of perovskites are categorized in FIG. 5a. Intrinsic point defects such as halide or A-site cation vacancies in the bulk form shallow traps, but undercoordinated halide or metal ions on the surface can form deep traps[150]. Defects in MHPs are charged owing to their ionic nature, but can be neutralized by coordinate bonding or ionic bonding, unlike in covalently bonded inorganic semiconductors. Coordinate bonding is enabled by Lewis acid–base adduct chemistry[148,181]. Lone-pair electrons in an atom have been widely used to passivate charged defects in perovskite optoelectronic devices. The donor atoms in the molecules are mainly nitrogen (for example, in pyridine[181] and hexamethylenediamine, 2,2′-(ethylenedioxy)diethylamine[182]), oxygen (for example, in triphenylphosphine oxide (TPPO)[183], trifluoroacetate[42], 5-ammonium valeric acid[33] and 4-(2-aminoethyl)benzoic acid[184]) and sulfur (for example, in thiourea[185] and thiophene[181]).

Phosphine oxides can passivate a reduced-dimensional perovskite edge, and the P=O:Pb bond has higher binding energy (1.1 eV) than the S=O:Pb bond (0.8 eV)[183]. A low-dimensional perovskite with edges passivated using TPPO showed a high PLQY of around 97%[183]. The binding energies of tribenzylphosphine oxide (TBPO) and TPPO were compared on perovskite surfaces; their intermolecular interaction can affect the binding energy and the stability of passivation[186] (FIG. 5c). TBPO shows higher binding energy than TPPO on the perovskite surface, and the intermolecular $\pi - \pi$ conjugation of TBPO molecules increases the binding energy of TBPO dimers (−8.2 eV) on the perovskite surface compared with TPPO double molecules (−5.4 eV) owing to the strengthened interaction of delocalized electrons on the aromatic conjugation with binding sites on the perovskite[186].

Defect passivation agents with the optimal molecular configuration of oxygen donor (C=O) that include N–H show good binding energy (theophylline has −1.7 eV, caffeine has −1.3 eV and theobromine has −1.1 eV). All three include a xanthine core, a carbonyl group C=O: and N–H; hydrogen bonding between N–H in the imidazole ring and the halide of PbX_6^{2-} promotes binding of C=O: with a Pb-antisite defect[187] (FIG. 5d). The presence of an additional methyl group on nitrogen (in caffeine and theobromine) weakens hydrogen bonding and reduces the passivation effect[187]. The hydrogen bonding strength in nitrogen-donor molecules affects defect passivation (FIG. 5e). Two similar amino-functionalized passivation agents (hexamethylenediamine (HMDA) and 2,2′-(ethylenedioxy)diethylamine (EDEA)) were studied; the only difference is that EDEA has additional oxygen atoms in its carbon chain[182] (FIG. 5e). The introduction of oxygen in the amino-functionalized molecule weakens hydrogen bonding between organic cations, so EDEA has a larger binding energy (−1.65 eV) with a defect-bearing perovskite surface than HMDA (−1.21 eV) despite both molecules being able to passivate the halide vacancy by coordination bonding between Pb and N (REF.[182]). Another type of amino-functionalized passivation molecule with weakened hydrogen bonding (2,2′-[oxybis(ethylenoxy)]diethylamine) yielded PeLEDs with a high EQE of 21.6%[182].

Sulfur-bearing donor molecules including thiourea (TU), thioacetamide (TAA), thiosemicarbazide (TSC) and nitrogen-bearing donors (guanidine, GU) were compared on $CsSnI_3$ (FIG. 5f). TSC showed the highest binding energy (−0.70 eV with Sn^{2+} at the $CsSnI_3$ surface), and strong electrostatic attraction of the S=C–N functional group with Sn^{2+} (TU has −0.45, TAA has −0.52 and GU has −0.40 eV), correlated with a higher dipole–ion interaction (Lewis acid–base) of C=S:Sn^{2+}. TSC was more efficient at passivating defects than TU, TAA and GU[188]. All the surface-defect passivating molecules shown in FIG. 5c–f are summarized in Supplementary Table 1.

The interface between MHPs and charge-transport layers hosts interfacial defects in PeLEDs. Conventional acidic hole-injection layers made of PEDOT:PSS can etch the electrode and induce diffusion of metallic species to the interface, quenching the luminescence of MHPs.

The neutralization of the acidity of PEDOT:PSS[189], through a modification of the layer to obtain a perfluorinated ionomer (PFI)-enriched surface[25,190,191] or a higher concentration of PSS on the surface[192] or the inclusion of a LiF interlayer on top of PEDOT:PSS[193], effectively prevents exciton quenching. Additional poly(triarylamine) hole-transport interlayers are widely used on the PEDOT:PSS layer to reduce nonradiative losses[194]. However, defects can be easily generated at the top or bottom of the MHP layer during the deposition of these interlayers. Therefore, additional defect-passivating interlayers are required. Lewis base products (such as 1,3,5-tris(2-*N*-phenylbenzimidazolyl) benzene[195], ethylenediamine[196] and octylamine[18]) can be overcoated on the MHP layer to obtain high luminous efficiency. Moreover, a 1,3,5-tris(bromomethyl) benzene interlayer introduced under the MHP prevented nonradiative recombination and improved hole injection, resulting in a high EQE of 16.3% in large-area PeLEDs[8]. Passivation of both sides of the MHP through the use of dual interlayers of oxide-4-(triphenylsilyl)phenyl (TSPO1) at the top and bottom of PeNCs yielded an EQE of 18.7%[197].

Several passivation strategies have been used in PeLEDs. Guanidinium (GA^+; $(NH_2)_3C^+$) was doped into $FAPbBr_3$ PeNCs. The strong configurational entropic energy stabilizes the crystal structure[6,175], and GA^+ doping decreases the size of the PeNC, increasing charge confinement. GA^+ located on the nanocrystal surface stabilizes PeNCs by coordinating with surface bromide with increased hydrogen bonding. Coating 1,3,5-tris(bromomethyl)-2,4,6-triethylbenzene (TBTB) on PeNC films provides excess Br^- ions through debromination and hydrogenation processes; these ions passivate the interfacial defects between PeNCs and the electron-transport layer. Thanks to these defect engineering strategies, PeLEDs with EQEs of 23.4% were achieved[6].

To fabricate PeLEDs with high efficiency and long-term stability, a comprehensive strategy to manage charged defects is required. All kinds of charged defects must be sufficiently passivated during synthesis or crystal growth or neutralized after crystal formation. Additionally, the development of non-destructive in situ techniques to quantify the number of traps and characterize the defect types in MHPs will accelerate the use of MHPs in practical applications.

Perovskite light-emitting diodes

EL-type displays and lighting applications require LEDs that have high efficiency and long lifetime. In our roadmap (FIG. 2b), engineering the charge-transporting interfaces and increasing the outcoupling efficiency (η_{out}) are important technical tasks for EL-type applications. The interface between charge-injection and charge-transport layers affects the efficiency and stability of LEDs. Also, light extraction from PeLEDs must be considered, given the different optical properties of MHPs with respect to those of conventional OLEDs. Additionally, white or special lighting devices that exploit the easy colour tuneability of MHPs should be developed with high efficiency and stability for greenhouses and for human-centric lighting applications.

This section reviews important technical challenges and developments in PeLED engineering, including charge injecting and transporting interfaces, the outcoupling efficiency of LEDs, and operational and colour stability of PeLEDs (Supplementary information).

Interfaces between the change-injecting and charge-transporting layer and outcoupling efficiency. The EQE of LEDs is the ratio of the number of photons emitted from a device to the number of electrons injected into it, and $EQE = \Phi \times \eta_{out} \times \gamma$, where Φ is the quantum efficiency of luminescence and γ is a charge-balance factor[198]. Taking the charge balance into account, the interfaces between charge-injecting and charge-transporting layers are crucial to determine the EQE. Also, the charge-injection efficiency of LEDs with an emissive layer that has a deep-lying VBM like MHPs and inorganic QDs strongly depends on the energy barrier for hole injection, thus using a hole-injection layer with a high work function is important to minimize the energy barrier and facilitate hole injection[27].

MHPs have low binding energy and long diffusion length, so the charge carriers and excitons in the emissive layer can diffuse onto the interfaces between the charge-injection and charge-transport layers and easily dissociate, which compromises the luminescence[27]. Therefore, the ability of the charge injection or transport layer to block charge carriers or excitons is more important than in OLEDs. Also, the charge-transport layer below the perovskite emissive layer should provide a good crystallization template to reduce the interfacial defects and ensure high crystal quality of the MHP.

MHPs have deeper VBM than organic host materials in the emissive layer (for example, the VBM of $MAPbBr_3$ is 5.8 eV)[27], and so ways to align the energy levels to reduce the charge-injection energy barrier have been sought. To reduce the energy barrier at the interface between the hole-injection layer and the emissive layer, self-organized polymeric hole-injection layers have been used; they include PFI, which has a low surface energy into PEDOT:PSS. The polymers self-organize to form a gradually increasing ionization potential, and the surface ionization potential reaches 5.9 eV, so the energy barrier at the hole-injecting interface is minimized, and hole injection into the emissive layer is efficient[25,27]. The surface of the hole-injection layer enriched with PFI effectively blocks electrons and exciton quenching at the interface[25,190,191].

The interface between the charge-transport layer and the emissive layer can also affect the crystallization of MHPs. A basic ZnO electron-transport layer deprotonates the organic cations and provides additional energy to remove them from the interface. The result is a decrease in the activation energy for the phase transition from the intermediate phase to perovskite crystals, compared to other metal oxide electron-transport layers (such as TiO_x and SnO). As a result, highly efficient PeLEDs with an EQE of 19.6% were achieved using an ZnO/polyethylenimine ethoxylated (PEIE) electron-transport layer[199].

One critical factor determining the EQE of LEDs is the outcoupling efficiency from the device to the outside.

The classical ray optics model, which predicts that $\eta_{out} = 1/2n^2$, where n is the refractive index, limits the outcoupling efficiency of PeLEDs with a MHP emissive layer (refractive index of 2.2) to about 20%[200]. The major loss path is a waveguide mode caused by the mismatch between the refractive index of the perovskite (about 2.2) and that of other layers (for example, glass, with $n \approx 1.45$). However, the outcoupling efficiency of PeNCs that have lower refractive index than polycrystalline emissive layers was simulated to be as high as 30.2% in PeLEDs with the following structure: glass/ITO (70 nm)/hole-injection layer (45 nm)/PeNC emissive layer (n: 1.7, 50 nm)/interlayer (5 nm)/ETL (50 nm)/Al (100 nm)[6]. The optimal outcoupling efficiency calculated was 31.3% in polycrystalline $MAPbBr_3$ ($n = 2.2$, wavelength = 530 nm, FWHM = 25 nm) in a device with structure glass/ITO ($\lambda/4$)/HTL($\lambda/4$)/emissive layer (about 0 nm)/electron-transport layer ($\lambda/4$)/Al (REF.[201]). Also, photon recycling strongly increases the outcoupling efficiency and therefore has the potential to substantially increase light extraction in PeLEDs to a value much greater than the theoretical classical ray-optics limit[200]. The relatively small Stokes shift of MHPs enables the reabsorption of emitted photons that are trapped and waveguided in the substrate, and randomization of the photons' directions by photon recycling can increase the outcoupling efficiency potentially up to 100%[200].

Operational stability of PeLEDs. The instability of MHPs and the operational instability of PeLEDs are impediments to commercialization. Ambient conditions and photo-exposure readily degrade MHPs[183]; both processes are accelerated at high temperature[138]. The thermodynamic phase instability of MHPs enables the phase transition of the perovskite to a photo-inactive phase, leading to degradation of materials and devices[149]. PeNCs can also degrade through the detachment of surface ligands, followed by crystal agglomeration[138].

One of the main causes of operational degradation of PeLEDs is ion migration under an electric field; this process generates defects and destroys the crystal structure[202]. This problem is particularly severe in PeLEDs, because LEDs need a higher electric field for operation compared with solar cells. Ionic motion in MHPs is highly sensitive to temperature, so Joule heating within PeLEDs can accelerate device degradation[203,204] (Supplementary information). Furthermore, ion migration can cause charge accumulation and electrochemical reactions between migrated ions and charge-transporting materials or electrodes[205].

Compositional engineering can help to stabilize the crystal and reduce the number of defects. The incorporation of binary alkali cations (Cs^+ and Rb^+ in $FAPbI_3$) stabilizes the perovskite as a result of the different location of Cs^+ and Rb^+ ions, which are incorporated in the lattice and at grain boundaries, respectively; the increased Coulombic interactions between cations and octahedral frameworks reduces ion migration[206]. As a result, PeLEDs using binary cations have an increased T_{50} of around 60 hours at 10 mA cm^{-2} (REF.[206]).

Defect passivation and surface treatment of MHPs reduce the number of surface defects and can contribute to blocking ion migration in PeLEDs. The chemical structure of defect-passivation molecules has a strong influence on the operational stability of PeLEDs. When dicarboxlic acids are incorporated as an additive in a MHP emissive layer on a ZnO electron-transport layer in PeLEDs, an amidation process catalysed by the underlying ZnO eliminates the active organic ingredients in the emissive layer. This process stabilizes the interfacial contact at the emissive layer/ZnO interface, substantially increasing the T_{50} to about 682 hours at 20 mA cm^{-2} (REF.[207]).

Stable β-$CsPbI_3$ nanocrystals have been synthesized using poly(maleicanhydride-alt-1-octadecene) (PMA) and used for PeLEDs[5]. The chemical interaction of PMA with PbI_2 regulated the kinetics of crystallization of β-$CsPbI_3$, and Pb–O bonding reduced the formation of deep-trap Pb anti-site defects. The improved crystal quality of PeNCs extended the T_{50} of PeLEDs to 317 hours at 30 mA cm^{-2} (REF.[5]).

Dimensional tailoring of MHPs is an effective method of improving the operational stability of PeLEDs. Reduced-dimensional perovskites that include large organic cations have higher formation energy and are more stable against degradation under ambient and operational conditions compared to their 3D counterparts[183]. A vertically aligned phase-pure 2D perovskite film deposited using hot casting increased the T_{50} of PeLEDs to more than 14 hours at 2 V, with an initial radiance of 6 W sr^{-1} m^{-2} (REF.[208]).

Mixed 2D–3D perovskites can also result in PeLEDs with improved stability[139,149]. The incorporation of neutral benzylamine in 3D perovskites causes the formation of 2D–3D hybrid films in the form of a 3D-core/2D-shell structure via proton transfer, which reduces the number of traps and ion migration in the perovskite film[72]. The 2D–3D hybrid PeLEDs had a reduced initial luminance overshoot and an extended operational lifetime of T_{40} = 810 minutes, which is more than 21 times longer than for their conventional 3D counterparts (T_{40} = 38 minutes at 100 cd m^{-2})[139].

The salt-type additive phenethylammonium iodide (PEAI) is also effective to induce the formation of 2D–3D core–shell perovskite nanostructures, thus increasing the device lifetime. The addition of a small fraction of 2D perovskite into the 3D perovskite suppressed δ-phase formation, reduced defect density, and led to the formation of a surface-2D/bulk-3D nanostructure in the preferred orientation of $FAPbI_3$ (REFS.[149,209]). This core–shell 2D–3D MHP had an activation energy more than six times higher for ion migration, and showed an increase in T_{50} of more than 1,000 times (202.7 hours under constant voltage to emit an initial radiance of 10 W sr^{-1} m^{-2}) compared to conventional 3D or quasi-2D MHPs[149].

To achieve high-stability PeLEDs, strategies must be developed to increase the MHPs intrinsic stability, in terms of structural and phase stability, and their extrinsic stability against atmospheric conditions, light, heat and electric fields. Methods to increase the intrinsic stability include A-site cation engineering to increase the structural stability of 3D MHPs[206], the use of large organic cations to increase the formation energy of 2D MHPs[208],

and the use of mixed-dimensional MHPs[139,149]. Methods of increasing the extrinsic stability of MHPs include reducing the number of defects within the crystal and at the film surface and interface in LEDs during the crystal growth step, and defect passivation to increase resistance to degradation by atmospheric species[138]. In particular, as ion migration is a critical weak point for LED operation, the use of a core–shell-type emitter is an effective strategy for both PeNCs and polycrystalline MHPs to reduce ion migration and extend the operational lifetime of PeLEDs[139,149].

Conclusion and outlook

We have discussed the technical challenges and the roadmap for commercialization of MHP emitters in the display and lighting industries, and summarized important technical strategies in the development of MHPs and PeLEDs. The technical roadmap (FIG. 2b) forecasts a timeline of potential industrial applications of MHPs, including as PL-type (colour conversion) displays, EL-type (LED) displays, near-eye displays and general and special lightings, and sets priorities for the relevant necessary technologies considering the current state of the art, emphasizing challenges that remain in the development of MHPs and PeLEDs.

Although great progress has been achieved in MHPs and PeLEDs in a short time, several critical challenges remain, such as widening the colour gamut of MHPs, increasing their operational reliability, developing environmentally benign MHPs, and improving large-area production techniques[210] (the technical challenges related to environmentally benign perovskites and large-scale production are discussed in more detail in the Supplementary information). To conclude, we suggest strategies to resolve the major challenges that currently impede the use of MHPs and PeLEDs in applications such as PL and EL displays and general and special lighting (FIG. 6).

PL-type displays are the application that MHPs may reach first. The high extinction coefficient of MHPs makes them promising materials for colour-conversion layers for near-eye displays for AR and VR applications. To exploit the wide colour gamut of MHPs, the first task is to demonstrate high colour reproducibility with each

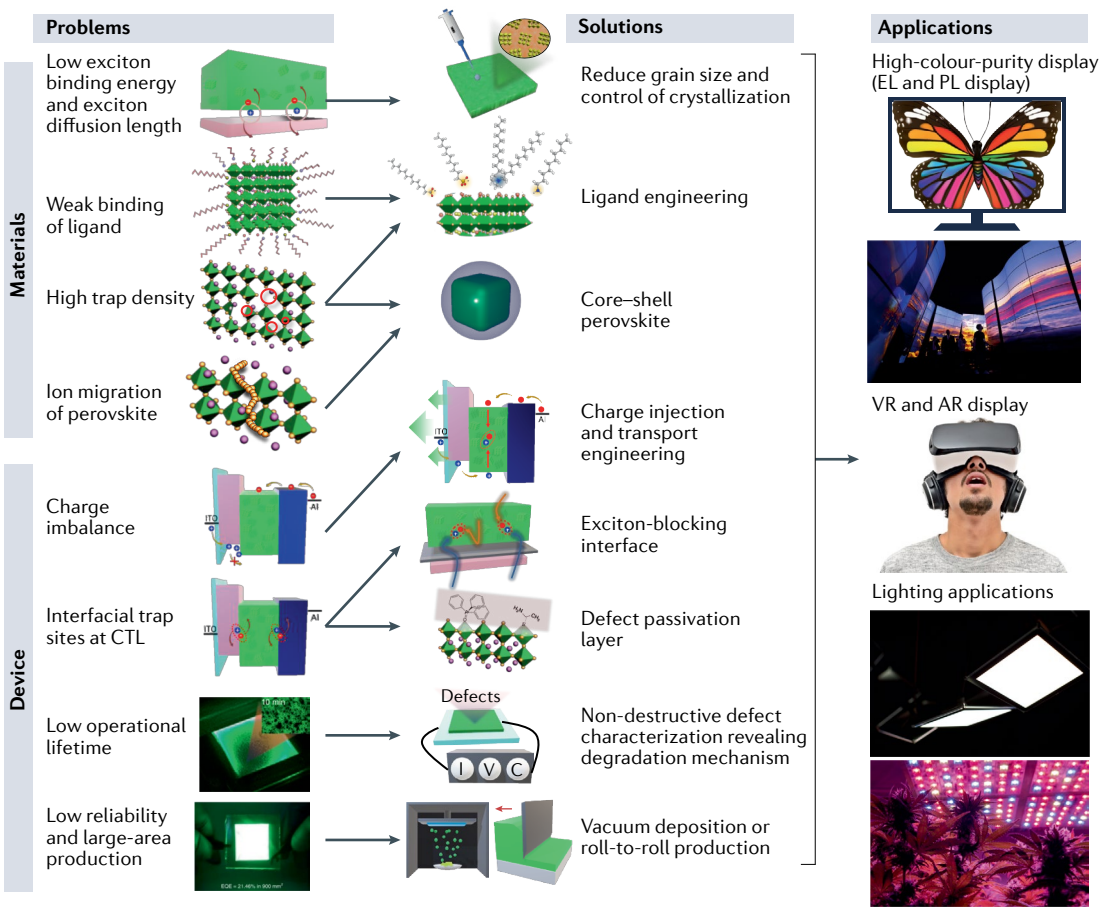

Fig. 6 | **Problems and solutions for perovskite light emitter applications.** Challenges for the application of perovskite materials and perovskite light-emitting diodes (LEDs), their potential solutions and the most promising future applications of perovskite light emitters. AR, augmented reality; CTL, charge-transport layer; EL, electroluminescence; PL, photoluminescence; VR, virtual reality. The picture of the green LED with degraded film is adapted with permission from REF.[240]. Copyright 2019 American Chemical Society. The picture of the bright green LED is adapted from REF.[241], Springer Nature Limited. Applications credit, top image: LPETTET/Getty Images; second image: Michele Tantussi/Stringer/Getty Images; third image: hocus-focus/Getty Images; fourth image, Bloomberg/Contributor/Getty Images; bottom image: Cavan Images/Getty Images.

colour-emitting MHP for both PL and EL displays. This outcome could be achieved using new large-scale synthesis processes and materials modification strategies to achieve the desired wavelengths and FWHM. To achieve spectral stability and high colour purity, the issue of halide segregation in mixed-halide MHP emitters must be solved[211,212].

Surface ligands and defect-passivating molecules on PeNCs and polycrystalline films will be important for defect passivation and to improve the electrical properties of MHPs, which directly translates into improved luminescence efficiency, storage lifetime of materials, operational lifetime of devices and processability. Therefore, achieving effective ligand and surface engineering will be a key step to overcome current technical limitations and to achieve high efficiency and long-term stability for both PL and EL applications. Recently, defect passivation using chelating agents for Pb^{2+} yielded PeLEDs with remarkable efficiency (ETPTA[213], with EQE of 22.49%, and reduced L-glutathione and EDTA[214], with EQE of 20.3%), respectively. These results suggest that new chelating materials that can effectively coordinate to Pb^{2+} will improve the characteristics of MHPs.

Currently, the biggest obstacle to commercialization of PeLEDs is the chemical instability of MHPs and of the devices that use them. Core–shell structuring of the emitter substantially reduces the number of surface traps, and increases both efficiency and stability. Therefore, the formation of films with core–shell-type grains or post-synthesis shelling of PeNCs may be an essential technology to increase the environmental stability and suppress ion migration in MHP emitters, thereby achieving high colour purity, high efficiency and long-term stability.

In LED devices, interfaces are important for high efficiency and stability. Charge injection and transport directly influence charge balance, and hence device efficiency and lifetime. In particular, MHPs have relatively low binding energy and long diffusion length compared to organic emitters in OLEDs, so the interface at MHP/charge-transport layers must be developed in a way that emphasizes blocking unwanted loss of charge carriers and excitons. Also, the surface of the MHP and interfacial layers should be modified to minimize the number of interfacial traps and non-radiative recombination paths.

Increasing the outcoupling efficiency of PeLEDs is an important strategy to improve device efficiency. Further study of the photon recycling effect in light extraction of PeLEDs may lead to its exploitation, potentially achieving outcoupling close to 100%.

Another advantage of MHPs is that they can be processed in vacuum, which is not the case for inorganic QDs. The path of development and commercialization of OLEDs in the display and lighting industries suggests that vacuum deposition is the most effective route to achieving reliable perovskite device operation. Most of the existing OLED production processes can be borrowed for MHPs, which means that the industrial transition from OLEDs to PeLEDs will be easier than that from LCDs to OLEDs. Therefore, research on vacuum-processed perovskite light emitters may be an important step towards commercialization.

The relatively soft nature of MHPs compared to other inorganic materials may lead to the development of flexible and stretchable LEDs, which will enable next-generation wearable high-colour-purity displays or special lighting. The development of flexible or stretchable PeLEDs will require appropriate engineering towards mechanically stable MHP films, along with the development of flexible and stretchable electrodes[215]; the combination of PeNCs with polymer matrices is a useful option[70].

Uniform and reliable high-resolution patterning of MHPs is required for PL and EL displays, as well as for near-eye displays. Although fine metal masks are widely used for patterning during vacuum deposition, photolithography can be used for solution-state materials; this method entails harsh conditions including ultraviolet exposure, O_2 plasma etching and polar solvents. Inkjet printing is another option for patterning, but it still has technical challenges regarding the nozzle design and the modulation of the ink's physical properties[216,217]. Therefore, a range of printing methods such as solution-free transfer printing[218], electrohydrodynamic printing[219] and non-destructive lithography[73,220,221] must be developed.

To follow the technical roadmap presented in this Review for the next 10 years, and to realize the commercialization of MHPs in the near future, further studies must be conducted to understand each process from the materials, device and processing points of view. MHP emitters have been developed much faster than have organic and QD emitters. Their potential applications are very broad, including new applications in VR and AR displays, biomedical displays, general and special lighting for smart farms as well as the more conventional applications in flat-panel displays, flexible displays and lighting. The current intense focus on MHPs and PeLEDs in academia and industry might even accelerate the progress anticipated in the roadmap.

Published online 4 August 2022

1. Lu, M. et al. Metal halide perovskite light-emitting devices: promising technology for next-generation displays. *Adv. Funct. Mater.* **29**, 1902008 (2019).
2. Dai, X., Deng, Y., Peng, X. & Jin, Y. Quantum-dot light-emitting diodes for large-area displays: towards the dawn of commercialization. *Adv. Mater.* **29**, 1607022 (2017).
3. Wang, Y. et al. All-inorganic quantum-dot LEDs based on a phase-stabilized α-$CsPbI_3$ perovskite. *Angew. Chem. Int. Ed.* **60**, 16164–16170 (2021).
4. Chiba, T. et al. Anion-exchange red perovskite quantum dots with ammonium iodine salts for highly efficient light-emitting devices. *Nat. Photon.* **12**, 681–687 (2018).
5. Li, H. et al. Efficient and stable red perovskite light-emitting diodes with operational stability >300 h. *Adv. Mater.* **33**, 2008820 (2021).
6. Kim, Y.-H. et al. Comprehensive defect suppression in perovskite nanocrystals for high-efficiency light-emitting diodes. *Nat. Photon.* **15**, 148–155 (2021).
7. Dong, Y. et al. Bipolar-shell resurfacing for blue LEDs based on strongly confined perovskite quantum dots. *Nat. Nanotechnol.* **15**, 668–674 (2020).
8. Wang, H. et al. A multi-functional molecular modifier enabling efficient large-area perovskite light-emitting diodes. *Joule* **4**, 1977–1987 (2020).
9. Hou, S., Gangishetty, M. K., Quan, Q. & Congreve, D. N. Efficient blue and white perovskite light-emitting diodes via manganese doping. *Joule* **2**, 2421–2433 (2018).
10. Karlsson, M. et al. Mixed halide perovskites for spectrally stable and high-efficiency blue light-emitting diodes. *Nat. Commun.* **12**, 361 (2021).
11. Protesescu, L. et al. Nanocrystals of cesium lead halide perovskites ($CsPbX_3$, X = Cl, Br, and I): novel optoelectronic materials showing bright

emission with wide color gamut. *Nano Lett.* **15**, 3692–3696 (2015).
12. Fang, Y., Dong, Q., Shao, Y., Yuan, Y. & Huang, J. Highly narrowband perovskite single-crystal photodetectors enabled by surface-charge recombination. *Nat. Photon.* **9**, 679–686 (2015).
13. Cho, H. et al. Overcoming the electroluminescence efficiency limitations of perovskite light-emitting diodes. *Science* **350**, 1222–1225 (2015).
14. Kumar, P. et al. Highly luminescent biocompatible $CsPbBr_3$@SiO_2 core–shell nanoprobes for bioimaging and drug delivery. *J. Mater. Chem. B* **8**, 10337–10345 (2020).
15. MacAdam, D. L. Visual sensitivities to color differences in daylight. *J. Opt. Soc. Am.* **32**, 247–274 (1942).
16. Wei, Z. & Xing, J. The rise of perovskite light-emitting diodes. *J. Phys. Chem. Lett.* **10**, 3035–3042 (2019).
17. Meloni, S., Palermo, G., Ashari-Astani, N., Grätzel, M. & Rothlisberger, U. Valence and conduction band tuning in halide perovskites for solar cell applications. *J. Mater. Chem. A* **4**, 15997–16002 (2016).
18. Shen, W. S. et al. Surfacial ligand management of a perovskite film for efficient and stable light-emitting diodes. *J. Mater. Chem. C* **7**, 14725–14730 (2019).
19. Yin, W.-J., Shi, T. & Yan, Y. Unusual defect physics in $CH_3NH_3PbI_3$ perovskite solar cell absorber. *Appl. Phys. Lett.* **104**, 63903 (2014).
20. Frost, J. M. et al. Atomistic origins of high-performance in hybrid halide perovskite solar cells. *Nano Lett.* **14**, 2584–2590 (2014).
21. Kim, H.-S. et al. Lead iodide perovskite sensitized all-solid-state submicron thin film mesoscopic solar cell with efficiency exceeding 9%. *Sci. Rep.* **2**, 591 (2012).
22. Milstein, T. J., Kroupa, D. M. & Gamelin, D. R. Picosecond quantum cutting generates photoluminescence quantum yields over 100% in ytterbium-doped $CsPbCl_3$ nanocrystals. *Nano Lett.* **18**, 3792–3799 (2018).
23. Herz, L. M. Charge-carrier dynamics in organic–inorganic metal halide perovskites. *Annu. Rev. Phys. Chem.* **67**, 65–89 (2016).
24. Stranks, S. D. et al. Electron-hole diffusion lengths exceeding 1 micrometer in an organometal trihalide perovskite absorber. *Science* **342**, 341–344 (2013).
25. Han, T.-H. et al. Molecularly controlled interfacial layer strategy toward highly efficient simple-structured organic light-emitting diodes. *Adv. Mater.* **24**, 1487–1493 (2012).
26. Han, T.-H. et al. Interface and defect engineering for metal halide perovskite optoelectronic devices. *Adv. Mater.* **31**, 1803515 (2019).
27. Kim, Y.-H. et al. Multicolored organic/inorganic hybrid perovskite light-emitting diodes. *Adv. Mater.* **27**, 1248–1254 (2015).
28. Yuan, M. et al. Perovskite energy funnels for efficient light-emitting diodes. *Nat. Nanotechnol.* **11**, 872–877 (2016).
29. Wright, A. D. et al. Electron–phonon coupling in hybrid lead halide perovskites. *Nat. Commun.* **7**, 11755 (2016).
30. Iaru, C. M., Geuchies, J. J., Koenraad, P. M., Vanmaekelbergh, D. & Silov, A. Y. Strong carrier–phonon coupling in lead halide perovskite nanocrystals. *ACS Nano* **11**, 11024–11030 (2017).
31. Tan, Z.-K. et al. Bright light-emitting diodes based on organometal halide perovskite. *Nat. Nanotechnol.* **9**, 687–692 (2014).
32. Lin, K. et al. Perovskite light-emitting diodes with external quantum efficiency exceeding 20 per cent. *Nature* **562**, 245–248 (2018).
33. Cao, Y. et al. Perovskite light-emitting diodes based on spontaneously formed submicrometre-scale structures. *Nature* **562**, 249–253 (2018).
34. Zhao, B. et al. Efficient light-emitting diodes from mixed-dimensional perovskites on a fluoride interface. *Nat. Electron.* **3**, 704–710 (2020).
35. Zhao, B. et al. High-efficiency perovskite–polymer bulk heterostructure light-emitting diodes. *Nat. Photon.* **12**, 783–789 (2018).
36. Zhang, Q. et al. Ceramic-like stable $CsPbBr_3$ nanocrystals encapsulated in silica derived from molecular sieve templates. *Nat. Commun.* **11**, 31 (2020).
37. Jang, J. et al. Extremely stable luminescent crosslinked perovskite nanoparticles under harsh environments over 1.5 years. *Adv. Mater.* **33**, 2005255 (2021).
38. Chang, S., Bai, Z. & Zhong, H. In situ fabricated perovskite nanocrystals: a revolution in optical materials. *Adv. Opt. Mater.* **6**, 1800380 (2018).
39. Zhou, Q. et al. In situ fabrication of halide perovskite nanocrystal-embedded polymer composite films with enhanced photoluminescence for display backlights. *Adv. Mater.* **28**, 9163–9168 (2016).
40. Forrest, S. R. *Organic Electronics: Foundations To Applications* (Oxford Univ. Press, 2020).
41. Woo, S.-J., Kim, J. S. & Lee, T.-W. Characterization of stability and challenges to improve operational lifetime in perovskite light-emitting diodes. *Nat. Photon.* **15**, 630–634 (2021).
42. Wang, H. et al. Trifluoroacetate induced small-grained $CsPbBr_3$ perovskite films result in efficient and stable light emitting devices. *Nat. Commun.* **10**, 665 (2019).
43. Liu, Y. et al. Bright and stable light-emitting diodes based on perovskite quantum dots in perovskite matrix. *J. Am. Chem. Soc.* **143**, 15606–15615 (2021).
44. Bi, C. et al. Perovskite quantum dots with ultralow trap density by acid etching-driven ligand exchange for high luminance and stable pure-blue light-emitting diodes. *Adv. Mater.* **33**, 2006722 (2021).
45. Cho, Y. J., Yook, K. S. & Lee, J. Y. High efficiency in a solution-processed thermally activated delayed-fluorescence device using a delayed-fluorescence emitting material with improved solubility. *Adv. Mater.* **26**, 6642–6646 (2014).
46. Lee, J. et al. Deep blue phosphorescent organic light-emitting diodes with very high brightness and efficiency. *Nat. Mater.* **15**, 92–98 (2016).
47. Sasabe, H. et al. High-efficiency blue and white organic light-emitting devices incorporating a blue iridium carbene complex. *Adv. Mater.* **22**, 5003–5007 (2010).
48. Kondo, Y. et al. Narrowband deep-blue organic light-emitting diode featuring an organoboron-based emitter. *Nat. Photon.* **13**, 678–682 (2019).
49. Yang, M., Park, I. S. & Yasuda, T. Full-color, narrowband, and high-efficiency electroluminescence from boron and carbazole embedded polycyclic heteroaromatics. *J. Am. Chem. Soc.* **142**, 19468–19472 (2020).
50. Yang, Y. et al. High-efficiency light-emitting devices based on quantum dots with tailored nanostructures. *Nat. Photon.* **9**, 259–265 (2015).
51. Kim, T. et al. Efficient and stable blue quantum dot light-emitting diode. *Nature* **586**, 385–389 (2020).
52. Shen, H. et al. Visible quantum dot light-emitting diodes with simultaneous high brightness and efficiency. *Nat. Photon.* **13**, 192–197 (2019).
53. Kim, Y.-H. et al. Highly efficient light-emitting diodes of colloidal metal-halide perovskite nanocrystals beyond quantum size. *ACS Nano* **11**, 6586–6593 (2017).
54. Kumar, S. et al. Ultrapure green light-emitting diodes using two-dimensional formamidinium perovskites: achieving recommendation 2020 color coordinates. *Nano Lett.* **17**, 5277–5284 (2017).
55. Zhang, S. et al. Efficient red perovskite light-emitting diodes based on solution-processed multiple quantum wells. *Adv. Mater.* **29**, 1606600 (2017).
56. DeRosa, M. C. et al. Synthesis, characterization, and evaluation of $[Ir(ppy)_2(vpy)Cl]$ as a polymer-bound oxygen sensor. *Inorg. Chem.* **42**, 4864–4872 (2003).
57. Wu, T. L. et al. Diboron compound-based organic light-emitting diodes with high efficiency and reduced efficiency roll-off. *Nat. Photon.* **12**, 235–240 (2018).
58. Zjang, Y., Baer, C. C. D., Camaioni-Neto, P. & O'Brien, D. A. S. A new synthetic route to the preparation of a series of strong photoreducing agents: fac tris-ortho-metalated complexes of iridium(III) with substituted 2-phenylpyridines. *Inorg. Chem.* **30**, 1685–1687 (1991).
59. Lee, K. H. et al. Over 40 cd/A efficient green quantum dot electroluminescent device comprising uniquely large-sized quantum dots. *ACS Nano* **8**, 4893–4901 (2014).
60. Li, Y. et al. Stoichiometry-controlled InP-based quantum dots: synthesis, photoluminescence, and electroluminescence. *J. Am. Chem. Soc.* **141**, 6448–6452 (2019).
61. Zhang, F. et al. Brightly luminescent and color-tunable colloidal $CH_3NH_3PbX_3$ (X = Br, I, Cl) quantum dots: potential alternatives for display technology. *ACS Nano* **9**, 4533–4542 (2015).
62. Lee, T.-W., Im, S. H., Kim, Y.-H. & Cho, H. Perovskite nanocrystal particle and optoelectronic device using the same. Patent KR-101815588-B1 (2018).
63. Won, Y. H. et al. Highly efficient and stable InP/ZnSe/ZnS quantum dot light-emitting diodes. *Nature* **575**, 634–638 (2019).
64. Maes, J. et al. Light absorption coefficient of $CsPbBr_3$ perovskite nanocrystals. *J. Phys. Chem. Lett.* **9**, 3093–3097 (2018).
65. Li, J., Chen, J., Shen, Y. & Peng, X. Extinction coefficient per CdE (E = Se or S) unit for zinc-blende CdE nanocrystals. *Nano Res.* **11**, 3991–4004 (2018).
66. Joung, J. F., Han, M., Jeong, M. & Park, S. Experimental database of optical properties of organic compounds. *Sci. Data* **7**, 295 (2020).
67. Talapin, D. V. et al. Etching of colloidal InP nanocrystals with fluorides: photochemical nature of the process resulting in high photoluminescence efficiency. *J. Phys. Chem. B* **106**, 12659–12663 (2002).
68. The European Parliament and The Council of The European Union. Directive 2011/65/EU of the European parliament and of the council of 8 June 2011 on the restriction of the use of certain hazardous substances in electrical and electronic equipment 88–110 (EU, 2011).
69. Bojan, T., Kumar, U. & Bojan, V. in *2014 IEEE Int. Conf. Vehicular Electron. Safety* 174–179 (IEEE, 2014).
70. Zhou, H. et al. Water passivation of perovskite nanocrystals enables air-stable intrinsically stretchable color-conversion layers for stretchable displays. *Adv. Mater.* **32**, 2001989 (2020).
71. Lee, T.-W., Im, S., Kim, Y.-H. & Cho, H. Perovskite nanocrystalline particles and optoelectronic device using same. US patent US-2017358757-A1 (2019).
72. Jang, H. J. et al. Progress of display performances: AR, VR, QLED, OLED, and TFT. *J. Inf. Disp.* **20**, 1–8 (2019).
73. Zou, C., Chang, C., Sun, D., Böhringer, K. F. & Lin, L. Y. Photolithographic patterning of perovskite thin films for multicolor display applications. *Nano Lett.* **20**, 3710–3717 (2020).
74. Kim, W. H. et al. High-performance color-converted full-color micro-LED arrays. *Appl. Sci.* **10**, 2112 (2020).
75. Lee, E. et al. Quantum dot conversion layers through inkjet printing. *SID Symp. Dig. Tech. Pap.* **49**, 525–527 (2018).
76. Yang, R. & Wang, W. A numerical and experimental study on gap compensation and wavelength selection in UV-lithography of ultra-high aspect ratio SU-8 microstructures. *Sens. Actuat. B* **110**, 279–288 (2005).
77. Morgan, M. G., Morgan, F. & Ine, B. The transition to solid-state lighting. *Proc. IEEE* **97**, 481–510 (2009).
78. Ooi, A. et al. Growth and development of Arabidopsis thaliana under single-wavelength red and blue laser light. *Sci. Rep.* **6**, 33885 (2016).
79. Morita, T. & Tokura, H. The influence of different wavelengths of light on human biological rhythms. *Appl. Hum. Sci.* **17**, 91–96 (1998).
80. Kim, Y.-H., Wolf, C., Kim, H. & Lee, T.-W. Charge carrier recombination and ion migration in metal-halide perovskite nanoparticle films for efficient light-emitting diodes. *Nano Energy* **52**, 329–335 (2018).
81. Park, J., Jang, H. M., Kim, S., Jo, S. H. & Lee, T.-W. Electroluminescence of perovskite nanocrystals with ligand engineering. *Trends Chem.* **2**, 837–849 (2020).
82. Lee, H. et al. Perovskite emitters as a platform material for down-conversion applications. *Adv. Mater. Technol.* **5**, 2000091 (2020).
83. Lee, T.-W., Kim, Y.-H. & Cho, H. Wavelength converting particle, method for manufacturing wavelength converting particle, and light emitting diode containing wavelength converting particle. US patent US-2020020834-A1 (2021).
84. Song, J. et al. Room-temperature triple-ligand surface engineering synergistically boosts ink stability, recombination dynamics, and charge injection toward EQE-11.6% perovskite QLEDs. *Adv. Mater.* **30**, 1800764 (2018).
85. Tong, Y. et al. Highly luminescent cesium lead halide perovskite nanocrystals with tunable composition and thickness by ultrasonication. *Angew. Chem. Int. Ed.* **55**, 13887–13892 (2016).
86. Hu, Y. L. et al. Rapid synthesis of cesium lead halide perovskite nanocrystals by l-lysine assisted solid-phase reaction at room temperature. *RSC Adv.* **10**, 34215–34224 (2020).
87. Kim, Y. et al. High efficiency perovskite light-emitting diodes of ligand-engineered colloidal formamidinium lead bromide nanoparticles. *Nano Energy* **38**, 51–58 (2017).
88. Li, D. et al. Improving stability of cesium lead iodide perovskite nanocrystals by solution surface treatments. *ACS Omega* **5**, 18013–18020 (2020).
89. Ripka, E. G., Deschene, C. R., Franck, J. M., Bae, I. T. & Maye, M. M. Understanding the surface properties of halide exchanged cesium lead halide nanoparticles. *Langmuir* **34**, 11139–11146 (2018).

90. Nenon, D. P. et al. Design principles for trap-free $CsPbX_3$ nanocrystals: enumerating and eliminating surface halide vacancies with softer lewis bases. *J. Am. Chem. Soc.* **140**, 17760–17772 (2018).
91. Zhang, F. et al. Colloidal synthesis of air-stable $CH_3NH_3PbI_3$ quantum dots by gaining chemical insight into the solvent effects. *Chem. Mater.* **29**, 3793–3799 (2017).
92. Nedelcu, G. et al. Fast anion-exchange in highly luminescent nanocrystals of cesium lead halide perovskites ($CsPbX_3$, X = Cl, Br, I). *Nano Lett.* **15**, 5635–5640 (2015).
93. Zhang, C. et al. Narrow-band violet-light-emitting diodes based on stable cesium lead chloride perovskite nanocrystals. *ACS Energy Lett.* **6**, 3545–3554 (2021).
94. Ma, D. et al. Chloride insertion-immobilization enables bright, narrowband, and stable blue-emitting perovskite diodes. *J. Am. Chem. Soc.* **142**, 5126–5513 (2020).
95. Shen, X. et al. Zn-alloyed $CsPbI_3$ nanocrystals for highly efficient perovskite light-emitting devices. *Nano Lett.* **19**, 1552–1559 (2019).
96. Almeida, G. et al. Role of acid-base equilibria in the size, shape, and phase control of cesium lead bromide nanocrystals. *ACS Nano* **12**, 1704–1711 (2018).
97. Lu, M. et al. Bright $CsPbI_3$ perovskite quantum dot light-emitting diodes with top-emitting structure and a low efficiency roll-off realized by applying zirconium acetylacetonate surface modification. *Nano Lett.* **20**, 2829–2836 (2020).
98. Zhang, J. et al. Enhancing stability of red perovskite nanocrystals through copper substitution for efficient light-emitting diodes. *Nano Energy* **62**, 434–441 (2019).
99. Song, J. et al. Organic–inorganic hybrid passivation enables perovskite QLEDs with an EQE of 16.48%. *Adv. Mater.* **30**, 1805409 (2018).
100. Chen, H. et al. High-efficiency formamidinium lead bromide perovskite nanocrystal-based light-emitting diodes fabricated via a surface defect self-passivation strategy. *Adv. Opt. Mater.* **8**, 1901390 (2020).
101. Chiba, T. et al. Neodymium chloride-doped perovskite nanocrystals for efficient blue light-emitting devices. *ACS Appl. Mater. Interf.* **12**, 53891–53898 (2020).
102. Yang, F. et al. Efficient and spectrally stable blue perovskite light-emitting diodes based on potassium passivated nanocrystals. *Adv. Funct. Mater.* **30**, 1908760 (2020).
103. Wang, Q. et al. Qualifying composition dependent p and n self-doping in $CH_3NH_3PbI_3$. *Appl. Phys. Lett.* **105**, 163508 (2014).
104. Xiao, Z. et al. Giant switchable photovoltaic effect in organometal trihalide perovskite devices. *Nat. Mater.* **14**, 193–197 (2015).
105. Jin, H. et al. It's a trap! on the nature of localised states and charge trapping in lead halide perovskites. *Mater. Horiz.* **7**, 397–410 (2020).
106. Zu, F. S. et al. Impact of white light illumination on the electronic and chemical structures of mixed halide and single crystal perovskites. *Adv. Opt. Mater.* **5**, 1700139 (2017).
107. Yong, Z. J. et al. Doping-enhanced short-range order of perovskite nanocrystals for near-unity violet luminescence quantum yield. *J. Am. Chem. Soc.* **140**, 9942–9951 (2018).
108. Akkerman, Q. A., Meggiolaro, D., Dang, Z., De Angelis, F. & Manna, L. Fluorescent alloy $CsPb_xMn_{1-x}I_3$ perovskite nanocrystals with high structural and optical stability. *ACS Energy Lett.* **2**, 2183–2186 (2017).
109. Behera, R. K. et al. Doping the smallest shannon radii transition metal ion Ni(II) for stabilizing α-$CsPbI_3$ perovskite nanocrystals. *J. Phys. Chem. Lett.* **10**, 7916–7921 (2019).
110. Woo, J. Y. et al. Highly stable cesium lead halide perovskite nanocrystals through in situ lead halide inorganic passivation. *Chem. Mater.* **29**, 7088–7092 (2017).
111. Bi, C. et al. Thermally stable copper(II)-doped cesium lead halide perovskite quantum dots with strong blue emission. *J. Phys. Chem. Lett.* **10**, 943–952 (2019).
112. Phung, N. et al. The doping mechanism of halide perovskite unveiled by alkaline earth metals. *J. Am. Chem. Soc.* **142**, 2364–2374 (2020).
113. Meggiolaro, D., Mosconi, E. & De Angelis, F. Formation of surface defects dominates ion migration in lead-halide perovskites. *ACS Energy Lett.* **4**, 779–785 (2019).
114. De Roo, J. et al. Highly dynamic ligand binding and light absorption coefficient of cesium lead bromide perovskite nanocrystals. *ACS Nano* **10**, 2071–2081 (2016).
115. Grisorio, R. et al. Exploring the surface chemistry of cesium lead halide perovskite nanocrystals. *Nanoscale* **11**, 986–999 (2019).
116. Hassanabadi, E. et al. Ligand and band gap engineering: tailoring the protocol synthesis for achieving high-quality $CsPbI_3$ quantum dots. *Nanoscale* **12**, 14194–14203 (2020).
117. Yao, J. S. et al. Suppressing Auger recombination in cesium lead bromide perovskite nanocrystal film for bright light-emitting diodes. *J. Phys. Chem. Lett.* **11**, 9371–9378 (2020).
118. Yao, J. et al. Calcium-tributylphosphine oxide passivation enables the efficiency of pure-blue perovskite light-emitting diode up to 3.3%. *Sci. Bull.* **65**, 1150–1153 (2020).
119. Fang, T. et al. Perovskite QLED with an external quantum efficiency of over 21% by modulating electronic transport. *Sci. Bull.* **66**, 36–43 (2021).
120. Li, J. et al. 50-Fold EQE mprovement up to 6.27% of solution-processed all-inorganic perovskite CsPbBr3 QLEDs via surface ligand density control. *Adv. Mater.* **29**, 1603885 (2017).
121. Hoshi, K. et al. Purification of perovskite quantum dots using low-dielectric-constant washing solvent 'diglyme' for highly efficient light-emitting devices. *ACS Appl. Mater. Interf.* **10**, 24607–24612 (2018).
122. Kumawat, N. K., Swarnkar, A., Nag, A. & Kabra, D. Ligand engineering to improve the luminance efficiency of $CsPbBr_3$ nanocrystal based light-emitting diodes. *J. Phys. Chem. C* **122**, 13767–13773 (2018).
123. Pan, J. et al. Highly efficient perovskite-quantum-dot light-emitting diodes by surface engineering. *Adv. Mater.* **28**, 8718–8725 (2016).
124. Pan, J. et al. Bidentate ligand-passivated $CsPbI_3$ perovskite nanocrystals for stable near-unity photoluminescence quantum yield and efficient red light-emitting diodes. *J. Am. Chem. Soc.* **140**, 562–565 (2018).
125. Krieg, F. et al. Colloidal $CsPbX_3$ (X = Cl, Br, I) nanocrystals 2.0: zwitterionic capping ligands for improved durability and stability. *ACS Energy Lett.* **3**, 641–646 (2018).
126. Zhang, B. et al. Alkyl phosphonic acids deliver $CsPbBr_3$ nanocrystals with high photoluminescence quantum yield and truncated octahedron shape. *Chem. Mater.* **31**, 9140–9147 (2019).
127. Brown, A. A. M. et al. Self-assembly of a robust hydrogen-bonded octylphosphonate network on cesium lead bromide perovskite nanocrystals for light-emitting diodes. *Nanoscale* **11**, 12370–12380 (2019).
128. Wang, T., Li, X., Fang, T., Wang, S. & Song, J. Room-temperature synthesis of perovskite-phase $CsPbI_3$ nanocrystals for optoelectronics via a ligand-mediated strategy. *Chem. Eng. J.* **418**, 129361 (2021).
129. Yang, D. et al. CsPbBr3 quantum dots 2.0: benzenesulfonic acid equivalent ligand awakens complete purification. *Adv. Mater.* **31**, 1900767 (2019).
130. Zhang, F. et al. Synergetic effect of the surfactant and silica coating on the enhanced emission and stability of perovskite quantum dots for anticounterfeiting. *ACS Appl. Mater. Interf.* **11**, 28013–28022 (2019).
131. Tang, B. et al. A universal synthesis strategy for stable $CsPbX_3$@oxide core–shell nanoparticles through bridging ligands. *Nanoscale* **13**, 10600–10607 (2021).
132. Zhong, Q. et al. One-pot synthesis of highly stable $CsPbBr_3$@SiO_2 core–shell nanoparticles. *ACS Nano* **12**, 8579–8587 (2018).
133. Huang, Y. et al. Enhancing the stability of $CH_3NH_3PbBr_3$ nanoparticles using double hydrophobic shells of SiO_2 and poly(vinylidene fluoride). *ACS Appl. Mater. Interf.* **11**, 26384–26391 (2019).
134. Loiudice, A., Strach, M., Saris, S., Chernyshov, D. & Buonsanti, R. Universal oxide shell growth enables in situ structural studies of perovskite nanocrystals during the anion exchange reaction. *J. Am. Chem. Soc.* **141**, 8254–8263 (2020).
135. Li, Z. J. et al. Photoelectrochemically active and environmentally stable $CsPbBr_3/TiO_2$ core/shell nanocrystals. *Adv. Funct. Mater.* **28**, 1704288 (2018).
136. Rainò, G. et al. Underestimated effect of a polymer matrix on the light emission of single $CsPbBr_3$ nanocrystals. *Nano Lett.* **19**, 3648–3653 (2019).
137. Shi, Z. et al. Strategy of solution-processed all-inorganic heterostructure for humidity/temperature-stable perovskite quantum dot light-emitting diodes. *ACS Nano* **12**, 1462–1472 (2018).
138. Cho, H., Kim, Y.-H., Wolf, C., Lee, H. D. & Lee, T.-W. Improving the stability of metal halide perovskite materials and light-emitting diodes. *Adv. Mater.* **30**, 1704587 (2018).
139. Kim, H. et al. Proton-transfer-induced 3D/2D hybrid perovskites suppress ion migration and reduce luminance overshoot. *Nat. Commun.* **11**, 3378 (2020).
140. Han, B. et al. Green perovskite light-emitting diodes with 200 hours stability and 16% efficiency: cross-linking strategy and mechanism. *Adv. Funct. Mater.* **31**, 2011003 (2021).
141. Minotto, A. et al. Role of core–shell interfaces on exciton recombination in CdSe-$Cd_xZn_{1-x}S$ quantum dots. *J. Phys. Chem. C* **118**, 24117–24126 (2014).
142. He, Y. et al. Suppression of the Auger recombination process in CdSe/CdS core/shell nanocrystals. *ACS Omega* **4**, 9198–9203 (2019).
143. Smith, A. M., Mohs, A. M. & Nie, S. Tuning the optical and electronic properties of colloidal nanocrystals by lattice strain. *Nat. Nanotechnol.* **4**, 56–63 (2009).
144. Li, G. et al. Highly efficient perovskite nanocrystal light-emitting diodes enabled by a universal crosslinking method. *Adv. Mater.* **28**, 3528–3534 (2016).
145. Tang, X. et al. Single halide perovskite/semiconductor core/shell quantum dots with ultrastability and nonblinking properties. *Adv. Sci.* **6**, 1900412 (2019).
146. Zhang, X. et al. PbS capped $CsPbI_3$ nanocrystals for efficient and stable light-emitting devices using p-i-n structures. *ACS Cent. Sci.* **4**, 1352–1359 (2018).
147. Zhang, C. et al. Core/shell perovskite nanocrystals: synthesis of highly efficient and environmentally stable $FAPbBr_3/CsPbBr_3$ for LED applications. *Adv. Funct. Mater.* **30**, 1910582 (2020).
148. Han, T.-H. et al. Perovskite-polymer composite cross-linker approach for highly-stable and efficient perovskite solar cells. *Nat. Commun.* **10**, 520 (2019).
149. Han, T.-H. et al. Surface-2D/bulk-3D heterophased perovskite nanograins for long-term-stable light-emitting diodes. *Adv. Mater.* **32**, 1905674 (2020).
150. Chen, B., Rudd, P. N., Yang, S., Yuan, Y. & Huang, J. Imperfections and their passivation in halide perovskite solar cells. *Chem. Soc. Rev.* **48**, 3842–3867 (2019).
151. Tanaka, K. et al. Comparative study on the excitons in lead-halide-based perovskite-type crystals $CH_3NH_3PbBr_3$ $CH_3NH_3PbI_3$. *Solid. State Commun.* **127**, 619–623 (2003).
152. Ding, B. et al. Material nucleation/growth competition tuning towards highly reproducible planar perovskite solar cells with efficiency exceeding 20%. *J. Mater. Chem. A* **5**, 6840–6848 (2017).
153. Park, M.-H. et al. Efficient perovskite light-emitting diodes using polycrystalline core–shell-mimicked nanograins. *Adv. Funct. Mater.* **29**, 1902017 (2019).
154. Si, J. et al. Efficient and high-color-purity light-emitting diodes based on in situ grown films of $CsPbX_3$ (X = Br, I) nanoplates with controlled thicknesses. *ACS Nano* **11**, 11100–11107 (2017).
155. Han, D. et al. Efficient light-emitting diodes based on in situ fabricated $FAPbBr_3$ nanocrystals: the enhancing role of the ligand-assisted reprecipitation process. *ACS Nano* **12**, 8808–8816 (2018).
156. Xiao, Z. et al. Efficient perovskite light-emitting diodes featuring nanometre-sized crystallites. *Nat. Photon.* **11**, 108–115 (2017).
157. Lee, H.-D. et al. Efficient Ruddlesden–Popper perovskite light-emitting diodes with randomly oriented nanocrystals. *Adv. Funct. Mater.* **29**, 1901225 (2019).
158. Byun, J. et al. Efficient visible quasi-2D perovskite light-emitting diodes. *Adv. Mater.* **28**, 7515–7520 (2016).
159. Zou, W. et al. Minimising efficiency roll-off in high-brightness perovskite light-emitting diodes. *Nat. Commun.* **9**, 608 (2018).
160. Chang, J. et al. Enhanced performance of red perovskite light-emitting diodes through the dimensional tailoring of perovskite multiple quantum wells. *J. Phys. Chem. Lett.* **9**, 881–886 (2018).
161. Wang, N. et al. Perovskite light-emitting diodes based on solution-processed self-organized multiple quantum wells. *Nat. Photon.* **10**, 699–704 (2016).
162. Sun, C. et al. High-performance large-area quasi-2D perovskite light-emitting diodes. *Nat. Commun.* **12**, 2207 (2021).
163. Xing, G. et al. Transcending the slow bimolecular recombination in lead-halide perovskites for electroluminescence. *Nat. Commun.* **8**, 14558 (2017).
164. Quan, L. N. et al. Tailoring the energy landscape in quasi-2D halide perovskites enables efficient green-light emission. *Nano Lett.* **17**, 3701–3709 (2017).

165. Liu, Y. et al. Efficient blue light-emitting diodes based on quantum-confined bromide perovskite nanostructures. *Nat. Photon.* **13**, 760–764 (2019).
166. Wang, C. et al. Dimension control of in situ fabricated $CsPbClBr_3$ nanocrystal films toward efficient blue light-emitting diodes. *Nat. Commun.* **11**, 6428 (2020).
167. Domanski, K. et al. Migration of cations induces reversible performance losses over day/night cycling in perovskite solar cells. *Energy Environ. Sci.* **10**, 604–613 (2017).
168. Yuan, Y. et al. Anomalous photovoltaic effect in organic-inorganic hybrid perovskite solar cells. *Sci. Adv.* **3**, e1602164 (2017).
169. Kang, D.-H. & Park, N.-G. On the current–voltage hysteresis in perovskite solar cells: dependence on perovskite composition and methods to remove hysteresis. *Adv. Mater.* **31**, 1805214 (2019).
170. Goldschmidt, V. M. Die Gesetze der Krystallochemie. *Naturwissenschaften* **14**, 477–485 (1926).
171. Amat, A. et al. Cation-induced band-gap tuning in organohalide perovskites: interplay of spin-orbit coupling and octahedra tilting. *Nano Lett.* **14**, 3608–3616 (2014).
172. Swarnkar, A., Mir, W. J. & Nag, A. Can B-site doping or alloying improve thermal- and phase-stability of all-inorganic $CsPbX_3$ (X = Cl, Br, I) perovskites? *ACS Energy Lett.* **3**, 286–289 (2018).
173. Ahmed, G. H., Yin, J., Bakr, O. M. & Mohammed, O. F. Near-unity photoluminescence quantum yield in inorganic perovskite nanocrystals by metal-ion doping. *J. Chem. Phys.* **152**, 020902 (2020).
174. Li, Z. et al. Stabilizing perovskite structures by tuning tolerance factor: formation of formamidinium and cesium lead iodide solid-state alloys. *Chem. Mater.* **28**, 284–292 (2016).
175. Yi, C. et al. Entropic stabilization of mixed A-cation ABX_3 metal halide perovskites for high performance perovskite solar cells. *Energy Environ. Sci.* **9**, 656–662 (2016).
176. Yin, J., Ahmed, G. H., Bakr, O. M., Brédas, J. L. & Mohammed, O. F. Unlocking the effect of trivalent metal doping in all-inorganic $CsPbBr_3$ perovskite. *ACS Energy Lett.* **4**, 789–795 (2019).
177. Yao, J. S. et al. Ce^{3+}-doping to modulate photoluminescence kinetics for efficient $CsPbBr_3$ nanocrystals based light-emitting diodes. *J. Am. Chem. Soc.* **140**, 3626–3634 (2018).
178. Wang, Q. et al. Efficient sky-blue perovskite light-emitting diodes via photoluminescence enhancement. *Nat. Commun.* **10**, 5633 (2019).
179. Yang, J. N. et al. Potassium bromide surface passivation on $CsPbI_{3-x}Br_x$ nanocrystals for efficient and stable pure red perovskite light-emitting diodes. *J. Am. Chem. Soc.* **142**, 2956–2967 (2020).
180. Chen, J. K. et al. High-efficiency violet-emitting all-inorganic perovskite nanocrystals enabled by alkaline-earth metal passivation. *Chem. Mater.* **31**, 3974–3983 (2019).
181. Noel, N. K. et al. Enhanced photoluminescence and solar cell performance via lewis base passivation of organic–inorganic lead halide perovskites. *ACS Nano* **8**, 9815–9821 (2014).
182. Xu, W. et al. Rational molecular passivation for high-performance perovskite light-emitting diodes. *Nat. Photonics* **13**, 418–424 (2019).
183. Na Quan, L. et al. Edge stabilization in reduced-dimensional perovskites. *Nat. Commun.* **11**, 170 (2020).
184. Ren, Z. et al. High-performance blue perovskite light-emitting diodes enabled by efficient energy transfer between coupled quasi-2D perovskite layers. *Adv. Mater.* **33**, 2005570 (2021).
185. Lee, J.-W., Kim, H.-S. & Park, N.-G. Lewis acid–base adduct approach for high efficiency perovskite solar cells. *Acc. Chem. Res.* **49**, 311–319 (2016).
186. Li, H. et al. Intermolecular π–π conjugation self-assembly to stabilize surface passivation of highly efficient perovskite solar cells. *Adv. Mater.* **32**, 1907396 (2020).
187. Wang, R. et al. Constructive molecular configurations for surface-defect passivation of perovskite photovoltaics. *Science* **366**, 1509–1513 (2019).
188. Li, B. et al. Efficient passivation strategy on Sn related defects for high performance all-inorganic CsSnI3 perovskite solar cells. *Adv. Funct. Mater.* **31**, 2007447 (2021).
189. Ahn, S. et al. Synergistic molecular engineering of hole-injecting conducting polymers overcomes luminescence quenching in perovskite light-emitting diodes. *Adv. Opt. Mater.* **9**, 2100646 (2021).
190. Seo, H.-K. et al. Efficient flexible organic/inorganic hybrid perovskite light-emitting diodes based on graphene anode. *Adv. Mater.* **29**, 1605587 (2017).
191. Park, M.-H. et al. Unravelling additive-based nanocrystal pinning for high efficiency organic-inorganic halide perovskite light-emitting diodes. *Nano Energy* **42**, 157–165 (2017).
192. Peng, X. F. et al. Modified conducting polymer hole injection layer for high-efficiency perovskite light-emitting devices: enhanced hole injection and reduced luminescence quenching. *J. Phys. Chem. Lett.* **8**, 4691–4697 (2017).
193. Li, Z. et al. Modification of interface between PEDOT:PSS and perovskite film inserting an ultrathin LiF layer for enhancing efficiency of perovskite light-emitting diodes. *Org. Electron.* **81**, 105675 (2020).
194. Hoye, R. L. Z. et al. Identifying and reducing interfacial losses to enhance color-pure electroluminescence in blue-emitting perovskite nanoplatelet light-emitting diodes. *ACS Energy Lett.* **4**, 1181–1188 (2019).
195. Xiao, Z. et al. Enhancing the performance of perovskite light-emitting devices through 1,3,5-tris(2-*N*-phenylbenzimidazolyl)benzene interlayer incorporation. *RSC Adv.* **9**, 29037–29043 (2019).
196. Lee, S. et al. Amine-based passivating materials for enhanced optical properties and performance of organic-inorganic perovskites in light-emitting diodes. *J. Phys. Chem. Lett.* **8**, 1784–1792 (2017).
197. Xu, L. et al. A bilateral interfacial passivation strategy promoting efficiency and stability of perovskite quantum dot light-emitting diodes. *Nat. Commun.* **11**, 3902 (2020).
198. Kumar, A., Srivastava, R., Kamalasanan, M. N. & Mehta, D. S. Enhancement of light extraction efficiency of organic light emitting diodes using nanostructured indium tin oxide. *Opt. Lett.* **37**, 575–577 (2012).
199. Yuan, Z. et al. Unveiling the synergistic effect of precursor stoichiometry and interfacial reactions for perovskite light-emitting diodes. *Nat. Commun.* **10**, 2818 (2019).
200. Cho, C. et al. The role of photon recycling in perovskite light-emitting diodes. *Nat. Commun.* **11**, 611 (2020).
201. Jeong, S.-H. et al. Characterizing the efficiency of perovskite solar cells and light-emitting diodes. *Joule* **4**, 1206–1235 (2020).
202. Zhao, L. et al. Electrical stress influences the efficiency of $CH_3NH_3PbI_3$ perovskite light emitting devices. *Adv. Mater.* **29**, 1605317 (2017).
203. Zhao, L. et al. Thermal management enables bright and stable perovskite light-emitting diodes. *Adv. Mater.* **32**, 2000752 (2020).
204. Zhao, L., Lee, K. M., Roh, K., Khan, S. U. Z. & Rand, B. P. Improved outcoupling efficiency and stability of perovskite light-emitting diodes using thin emitting layers. *Adv. Mater.* **31**, 1805836 (2019).
205. Guerrero, A. et al. Interfacial degradation of planar lead halide perovskite solar cells. *ACS Nano* **10**, 218–224 (2016).
206. Li, N. et al. Stabilizing perovskite light-emitting diodes by incorporation of binary alkali cations. *Adv. Mater.* **32**, 1907786 (2020).
207. Kuang, C. et al. Critical role of additive-induced molecular interaction on the operational stability of perovskite light-emitting diodes. *Joule* **5**, 618–630 (2021).
208. Tsai, H. et al. Stable light-emitting diodes using phase-pure Ruddlesden–Popper layered perovskites. *Adv. Mater.* **30**, 1704217 (2018).
209. Lee, J.-W. et al. Solid-phase hetero epitaxial growth of α-phase formamidinium perovskite. *Nat. Commun.* **11**, 5514 (2020).
210. Yang, M. et al. Perovskite ink with wide processing window for scalable high-efficiency solar cells. *Nat. Energy* **2**, 17038 (2017).
211. Muscarella, L. A. et al. Lattice compression increases the activation barrier for phase segregation in mixed-halide perovskites. *ACS Energy Lett.* **5**, 3152–3158 (2020).
212. Knight, A. J. & Herz, L. M. Preventing phase segregation in mixed-halide perovskites: a perspective. *Energy Environ. Sci.* **13**, 2024–2046 (2020).
213. Chu, Z. et al. Perovskite light-emitting diodes with external quantum efficiency exceeding 22% via small-molecule passivation. *Adv. Mater.* **33**, 2007169 (2021).
214. Hassan, Y. et al. Ligand-engineered bandgap stability in mixed-halide perovskite LEDs. *Nature* **591**, 72–77 (2021).
215. Lim, K.-G., Han, T.-H. & Lee, T.-W. Engineering electrodes and metal halide perovskite materials for flexible/stretchable perovskite solar cells and light-emitting diodes. *Energy Environ. Sci.* **14**, 2009–2035 (2021).
216. Shin, P., Sung, J. & Ho, M. Microelectronics reliability control of droplet formation for low viscosity fluid by double waveforms applied to a piezoelectric inkjet nozzle. *Microelectron. Reliab.* **51**, 797–804 (2011).
217. Gao, A. et al. Printable $CsPbBr_3$ perovskite quantum dot ink for coffee ring-free fluorescent microarrays using inkjet printing. *Nanoscale* **12**, 2569–2577 (2020).
218. Kim, T. et al. Full-colour quantum dot displays fabricated by transfer printing. *Nat. Photon.* **5**, 176–182 (2011).
219. Cui, Z., Han, Y., Huang, Q., Dong, J. & Zhu, Y. Electrohydrodynamic printing of silver nanowires for flexible and stretchable electronics. *Nanoscale* **10**, 6806–6811 (2018).
220. Lee, W. et al. High-resolution spin-on-patterning of perovskite thin films for a multiplexed image sensor array. *Adv. Mater.* **29**, 1702902 (2017).
221. Lin, C. H. et al. Large-area lasing and multicolor perovskite quantum dot patterns. *Adv. Opt. Mater.* **6**, 1800474 (2018).
222. Hou, S., Guo, Y., Tang, Y. & Quan, Q. Synthesis and stabilization of colloidal perovskite nanocrystals by multidentate polymer micelles. *ACS Appl. Mater. Interf.* **9**, 18417–18422 (2017).
223. Li, H., Jia, C., Li, H. & Meng, X. $CsPbX_3/Cs_4PbX_6$ core/shell perovskite nanocrystals. *Chem. Commun.* **54**, 6300–6303 (2018).
224. Wang, B. et al. Postsynthesis phase transformation for $CsPbBr_3/Rb_4PbBr_6$ core/shell nanocrystals with exceptional photostability. *ACS Appl. Mater. Interf.* **10**, 23303–23310 (2018).
225. Zhao, H. et al. High-brightness perovskite light-emitting diodes based on $FAPbBr_3$ nanocrystals with rationally designed aromatic ligands. *ACS Energy Lett.* **6**, 2395–2403 (2021).
226. Fang, Z. et al. Dual passivation of perovskite defects for light-emitting diodes with external quantum efficiency exceeding 20%. *Adv. Funct. Mater.* **30**, 1909754 (2020).
227. Liu, Z. et al. Perovskite light-emitting diodes with EQE exceeding 28% through a synergetic dual-additive strategy for defect passivation and nanostructure regulation. *Adv. Mater.* **33**, 2103268 (2021).
228. Chu, S. et al. Large-area and efficient perovskite light-emitting diodes via low-temperature blade-coating. *Nat. Commun.* **12**, 147 (2021).
229. Ma, D. et al. Distribution control enables efficient reduced-dimensional perovskite LEDs. *Nature* **599**, 594–598 (2021).
230. Jiang, Y. et al. Reducing the impact of Auger recombination in quasi-2D perovskite light-emitting diodes. *Nat. Commun.* **12**, 336 (2021).
231. Liu, Y. et al. Water-soluble conjugated polyelectrolyte hole transporting layer for efficient sky-blue perovskite light-emitting diodes. *Small* **17**, 1–8 (2021).
232. Dai, X. et al. Solution-processed, high-performance light-emitting diodes based on quantum dots. *Nature* **515**, 96–99 (2014).
233. Wang, L. et al. Blue quantum dot light-emitting diodes with high electroluminescent efficiency. *ACS Appl. Mater. Interf.* **9**, 38755–38760 (2017).
234. Xu, Y. et al. Constructing charge-transfer excited states based on frontier molecular orbital engineering: narrowband green electroluminescence with high color purity and efficiency. *Angew. Chem. Int. Ed.* **132**, 17595–17599 (2020).
235. Woo Choi, J. et al. Organic–inorganic hybrid perovskite quantum dots with high PLQY and enhanced carrier mobility through crystallinity control by solvent engineering and solid-state ligand exchange. *Nanoscale* **10**, 13356–13367 (2018).
236. Salas, G., Costo, R. & del Puerto Morales, M. Synthesis of inorganic nanoparticles. *Front. Nanosci.* **4**, 35–79 (2012).
237. Thanh, N. T. K., Maclean, N. & Mahiddine, S. Mechanisms of nucleation and growth of nanoparticles in solution. *Chem. Rev.* **114**, 7610–7630 (2014).
238. Kim, B. W. et al. Morphology controlled nanocrystalline $CsPbBr_3$ thin-film for metal halide perovskite light emitting diodes. *J. Ind. Eng. Chem.* **97**, 417–425 (2021).

239. Huang, G. et al. A strategy for improving the performance of perovskite red light-emitting diodes by controlling the growth of perovskite crystal. *J. Mater. Chem. C* **7**, 11887–11895 (2019).
240. Lee, H., Ko, D. & Lee, C. Direct evidence of ion-migration-induced degradation of ultrabright perovskite light-emitting diodes. *ACS Appl. Mater. Interf.* **11**, 11667–11673 (2019).
241. Kim, Y. et al. Exploiting the full advantages of colloidal perovskite nanocrystals for large-area efficient light-emitting diodes. *Nat. Nanotechnol.* **17**, 590–597 (2022).

Acknowledgements
This work was supported by National Research Foundation of Korea (NRF) grants funded by the Korea government (MSIT) (grant numbers NRF-2016R1A3B1908431 and 2020R1C1C1008485). This research was also supported by the Creative Materials Discovery Program through the NRF, funded by the Ministry of Science and ICT (grant number 2018M3D1A1058536). K.Y.J. acknowledged the support from the Korea Institute of Energy Technology Evaluation and Planning (KETEP) grant funded by the Korea government (MOTIE) (grant number 20214000000570).

Author contributions
T.-H.H. and K.Y.J. researched data for the article. T.-H.H., K.Y.J. and T.-W.L. contributed substantially to discussion of the content. T.-H.H., K.Y.J. and T.-W.L. wrote the article. All authors reviewed and/or edited the manuscript before submission.

Competing interests
The authors declare no competing interests.

Peer review information
Nature Reviews Materials thanks the anonymous reviewers for their contribution to the peer review of this work.

Publisher's note
Springer Nature remains neutral with regard to jurisdictional claims in published maps and institutional affiliations.

Springer Nature or its licensor holds exclusive rights to this article under a publishing agreement with the author(s) or other rightsholder(s); author self-archiving of the accepted manuscript version of this article is solely governed by the terms of such publishing agreement and applicable law.

Supplementary information
The online version contains supplementary material available at https://doi.org/10.1038/s41578-022-00459-4.

RELATED LINKS
ITU-R Recommendation BT.2020: https://www.itu.int/rec/R-REC-BT.2020-0-201208-S
LCD televisions based on perovskite-QD films: https://www.perovskite-info.com/tcl-and-zhijing-nanotech-collaborate-pqd-solutions-lcd-tvs
QDot LCD SharpGreen perovskite film: https://quantum-solutions.com/product/qdot-lcd-sharpgreen-perovskite-film/

© Springer Nature Limited 2022, corrected publication 2022